



**HAL**  
open science

## ECR–Driven Negative Ion Sources Operating with Hydrogen and Deuterium

P. Svarnas, M. Mitrou, J. Lemaire, L. Gavilan, N. de Oliveira, S. Béchu

► **To cite this version:**

P. Svarnas, M. Mitrou, J. Lemaire, L. Gavilan, N. de Oliveira, et al.. ECR–Driven Negative Ion Sources Operating with Hydrogen and Deuterium. Marthe Bacal. Physics and Applications of Hydrogen Negative Ion Sources, 124, Springer International Publishing, pp.303-347, 2023, Springer Series on Atomic, Optical, and Plasma Physics, 978-3-031-21475-2. 10.1007/978-3-031-21476-9\_12 . hal-04280385

**HAL Id: hal-04280385**

**<https://hal.science/hal-04280385>**

Submitted on 14 Nov 2023

**HAL** is a multi-disciplinary open access archive for the deposit and dissemination of scientific research documents, whether they are published or not. The documents may come from teaching and research institutions in France or abroad, or from public or private research centers.

L'archive ouverte pluridisciplinaire **HAL**, est destinée au dépôt et à la diffusion de documents scientifiques de niveau recherche, publiés ou non, émanant des établissements d'enseignement et de recherche français ou étrangers, des laboratoires publics ou privés.

# Chapter 12

## ECR–Driven Negative Ion Sources Operating with Hydrogen and Deuterium

P. Svarnas<sup>1†</sup>, M. Mitrou<sup>1,2</sup>, J. L. Lemaire<sup>3</sup>, L. Gavilan<sup>4</sup>, N de Oliveira<sup>5</sup> and S. Béchu<sup>2</sup>

<sup>1</sup> University of Patras, Electrical and Computer Engineering Department, High Voltage Lab., 26 504 Rion, Patras, Greece

<sup>2</sup> Université Grenoble Alpes, CNRS, Grenoble INP (Institute of Engineering), LPSC-IN2P3, 38 000 Grenoble, France

<sup>3</sup> Institut des Sciences Moléculaires d’Orsay (ISMO), CNRS-Université Paris-Sud (UMR8214), 91 405 Orsay, France

<sup>4</sup> Space Science and Astrobiology Division, NASA Ames Research Center, Moffett Field, CA 94 035, USA

<sup>5</sup> DESIRS beamline, Synchrotron SOLEIL, Saint Aubin, 91 192 Gif sur Yvette, France

† Corresponding Author: [svarnas@ece.upatras.gr](mailto:svarnas@ece.upatras.gr)

**Keywords:** ECR plasmas; hydrogen; deuterium; negative ions; ion sources; ion beams.

**Abstract:** The present chapter is devoted to the fundamental principles of electron cyclotron resonance (ECR) sources yielding  $H^-$  and  $D^-$  negative ions. Initially, it provides a brief but meaningful overview of the theoretical framework for ECR plasmas along with commonly employed experimental configurations, unveiling thus the distinct features of this special category of high frequency electrical discharges. It is highlighted that, it is not aimed to cover the vast field of microwave discharges (e.g., microwave discharges in waveguides and resonators), neither the vast field of wave-heated discharges (e.g., helicon discharges and surface wave discharges). Such an attempt would be an utopia within the frame of one book chapter. Therefore, the first section of the chapter presents elementary physical quantities of plasmas, related to the ECR idea, and an idealized, simplified concept of the complex wave propagation in ECR plasmas where the wave energy absorption is achieved through collisionless heating mechanism [Fridman and Kennedy 2004; Williamson *et al.* 1992]. The presentation concerns low pressure, nonthermal, and nonequilibrium plasmas. Then, the core of this review is devoted to the targeted application of ECR heating to negative ion sources operating with molecular hydrogen ( $H_2$ ) and deuterium ( $D_2$ ). Once again, the relative vast field is impossible to be treated in the context of this chapter, but the authors hope that the cited sources are worthy representatives. Fundamental processes governing the  $H^-$  and  $D^-$  ion production (destruction) are summarized in section 2, while the extended section 3 provides recent experimental results from ECR-driven sources and comments on them in detail. Diagnostic techniques applicable to these sources are also mentioned at the beginning of section 3. The chapter closes with section 4, where additional ECR sources are touched upon and negative ion extracted currents from different sources are compared. The review is throughout supported by future-proof classic or up-to-date bibliography for further reading.

### 12.1 Fundamental Principles of Electron Cyclotron Resonance (ECR) Heating<sup>(1)</sup>

Microwave generation of plasmas has been employed since the invention of high power, microwave sources in World War II. However, traditional microwave generation of plasmas has inherent limitations such as low critical plasma densities and requirement for high resonant microwave cavity quality factor [Lieberman and Lichtenberg 2005]. Analytically, the electron plasma frequency, i.e, the frequency with which electrons oscillate among the heavier, immobile ions when the electron population is disturbed, equals [Roth 1995]

$$\omega_{ep} = 2\pi \nu_{ep} = \sqrt{\frac{n_e e^2}{m_e \epsilon_0}} \quad \text{Eq. (1)}$$

If a plasma is irradiated with externally applied electromagnetic radiation of frequency  $\omega_0 = 2\pi \nu_0$ , there is a critical electron number density  $(n_e)_c$  below which the radiation will be transmitted through the plasma, otherwise if  $n_e$  exceeds  $(n_e)_c$ , the radiation will be reflected [Roth 1995]. This critical number density is the threshold for which  $\omega_0 = \omega_{ep}$ . As a

<sup>(1)</sup> It is evident that this section comprises an introductory text on the ECR (propagating wave) heating to facilitate the presentation of the ECR sources. Rigorous consideration of the ECR heating mechanisms (e.g., collisional vs. collisionless), magnetic field optimization, impedance matching issues etc. can be found in dedicated reports, e.g., [Williamson *et al.* 1992; Gammino *et al.* 2010; Asmussen and Mak 1994].

reminder, if  $\omega > \omega_{ep}$  the electrons have too much inertia to respond to the electric field of the wave, and the radiation can propagate through the plasma without significant reflection or attenuation, whereas, if  $\omega < \omega_{ep}$  the radiation will be reflected. Thus, substitution in **Eq. (1)** gives the formula below.

$$(n_e)_c = \frac{\omega_0^2 m_e \varepsilon_0}{e^2} = \frac{4 \pi^2 m_e \varepsilon_0}{e^2} \nu_0^2 \quad \text{Eq. (2)}$$

**Eqs. (1) and (2)** are graphically correlated in **Fig. 12.1**.

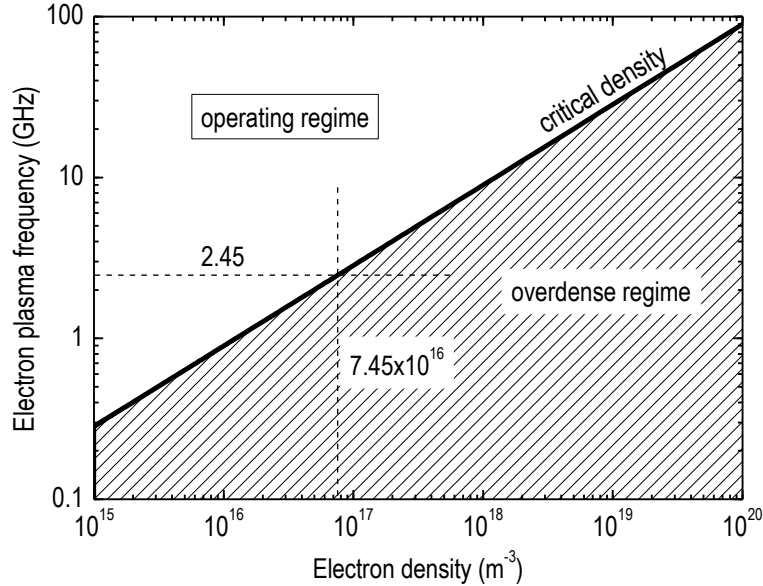


**Figure 12.1.** The solid line indicates the critical electron number density for different electron plasma frequencies. The widely used industrial frequency of 2.45 GHz is indicated and corresponds to a density of  $7.45 \times 10^{16} \text{ m}^{-3}$ . Over-dense plasmas are those below and to the right of the critical density. Redrawn from [Roth 1995].

The introduction of a steady state magnetic field **B**, in which there is a resonance between the externally applied frequency and the electron cyclotron frequency somewhere within the discharge, allows operation at high density and without a cavity resonance [Lieberman and Lichtenberg 2005]. The gyrating electrons rotate in phase with the right-hand circularly polarized wave, seeing a steady state electric field over many gyro-orbits. Thus, the high field of the cavity resonance, acting over a short time, is replaced by a much lower field, but acting over a much longer time. This leads to sufficient energy gain of the electrons to allow ionization of the background gas. Furthermore, the injection of the microwaves along the magnetic field, with electron gyrofrequency  $\omega_{ec} > \omega_0$  at the entry into the discharge region, allows wave propagation to the absorption zone  $\omega_{ec} \approx \omega_0$ , even in a dense plasma with  $\omega_{ep} > \omega_0$  [Lieberman and Lichtenberg 2005].

Strictly speaking [Roth 1995], the resonance in question is much closer to the upper hybrid frequency

$$\omega_{uh} = \sqrt{\omega_{ec}^2 + \omega_{ep}^2} \quad \text{Eq. (3)}$$

than to the electron gyrofrequency

$$\omega_{ec} = \frac{e B}{m_e} \quad \text{Eq. (4)}$$

This becomes more pronounced in plasmas of significant density (see **Eq. 1**).

In order to heat a magnetized plasma with the extraordinary mode of electromagnetic radiation [Roth 1995], i.e., the electric field vector is perpendicular to the confining magnetic field, incident radiation  $\omega_0 = 2\pi \nu_0$  at the electron gyrofrequency  $\omega_{ec} = 2\pi \nu_{ec}$  (i.e., consider the case where  $\nu_0 \approx \nu_{ec} < \nu_{uh}$ ) should be above the electron plasma frequency in order to penetrate the plasma and heat it throughout its volume without significant reflection or attenuation. Hence, this condition states that

$$\omega_{ec} \geq \omega_{ep} \Rightarrow \frac{e B}{m_e} \geq \sqrt{\frac{n_e e^2}{m_e \epsilon_0}} \quad \text{Eq. (5)}$$

and, solving for  $B$ , a lower limit for the magnetic induction required to apply ECR heating to a plasma with given electron density  $n_e$  is obtained, i.e.,

$$B \geq \sqrt{\frac{n_e m_e}{\epsilon_0}} \quad \text{Eq. (6)}$$

On the other hand, the power input to a magnetized plasma in the individual particle regime has a sharp maximum near the ECR frequency  $\omega_{ec} = 2\pi \nu_{ec}$ , given by **Eq. 4** as a function of the magnetic induction of the externally applied magnetic field [Roth 1995]. This dependence is presented in **Fig. 12.2**. For the widely used industrial frequency of 2.45 GHz, a magnetic induction of 87.5 mT is required, which is easily within reach of low power direct current electromagnets or permanent magnets.

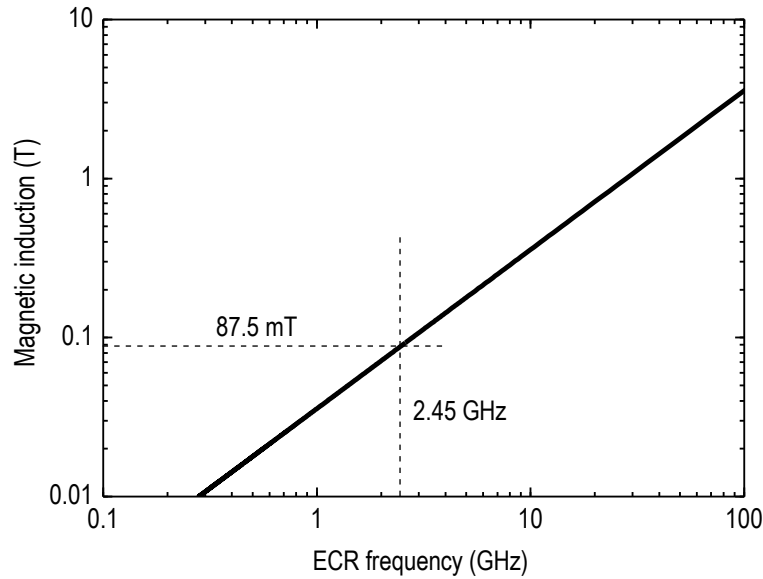


**Figure 12.2.** Magnetic induction requirement for fulfilling the ECR condition (Eq. 4) at different frequencies. The conventionally pair (2.45 GHz, 87.5 mT) is marked on the plot. Redrawn from [Roth 1995].

The basic principle of ECR heating is better explained in **Fig. 12.3** [Lieberman and Lichtenberg 2005]. A linearly polarized microwave field launched into the source chamber can be decomposed into the sum of two counter-rotating circularly polarized waves. Assuming a sinusoidal steady state with the incident wave polarized along  $\mathbf{x}_0$  ( $\mathbf{x}_0$  stands for the unit vector along the x-axis; similarly,  $\mathbf{y}_0$  is the unit vector along y-axis), i.e.,

$$\mathbf{E}(\mathbf{r}, t) = \mathbf{x}_0 E_x(\mathbf{r}) \cos(\omega_0 t) \quad \text{Eq. (7)}$$

where the complex amplitude  $E_x$  is here taken to be pure real, the resulting expression is

$$\mathbf{x}_0 E_x = (\mathbf{x}_0 - j \mathbf{y}_0) E_r + (\mathbf{x}_0 + j \mathbf{y}_0) E_l \quad \text{Eq. (8)}$$

where  $E_r$  and  $E_l$  are the amplitudes of the RHP and LHP waves, respectively, with  $E_r = E_l = E_x / 2$ . The electric field vector of the RHP wave rotates in the right-hand sense around the magnetic field at frequency  $\omega_0$  while an electron in a uniform magnetic field  $B_0$  also gyrates in a right-hand sense at frequency  $\omega_{ec}$ . Thus, as shown in **Fig. 12.3(a) – (d)**, for  $\omega_{ec} = \omega_0$ , the force  $F_E = -e E$  accelerates the electron along its circular orbit, resulting in a continuous transverse energy gain. On the other hand, as shown in **Fig. 12.3(e) – (h)**, the LHP wave field produces an oscillating force whose time average is zero, resulting in no energy gain.

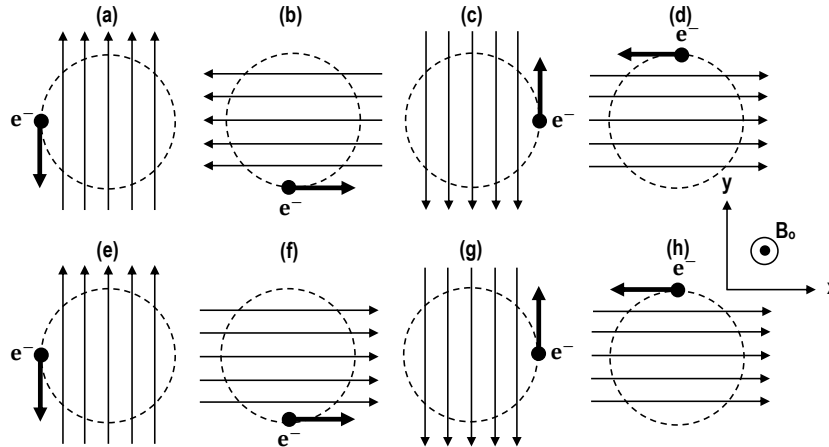


**Figure 12.3.** Basic principle of ECR heating. (a) – (d) Continuous energy gain for the RHP. (e) – (h) Oscillating energy for LHP: (e) gain; (f) loss; (g) gain; (h) loss. Redrawn from [Lieberman and Lichtenberg 2005].

From a practical point of view, a typical setup for generating power microwaves for ECR heating is presented in **Fig. 12.4**. In this figure, the microwave power delivery is based on a conventional 2.45 GHz magnetron system. More details on the individual components, can be found in previous references [Roth 1995]. Nowadays, solid state, fully controllable microwave power supplies are available (e.g., Sairem Ltd.).

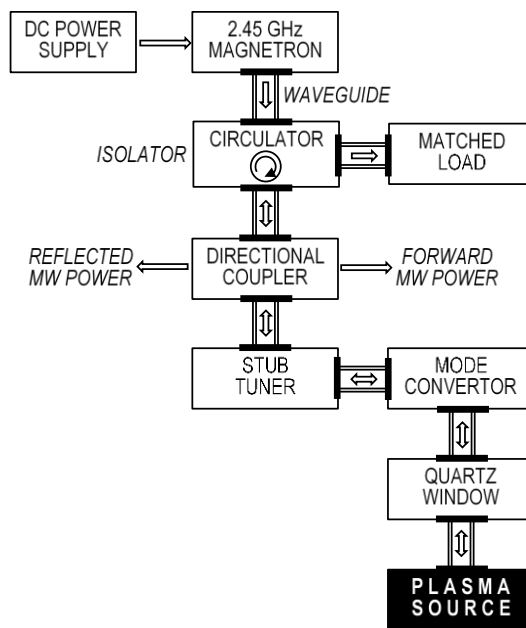


**Figure 12.4.** Conventional concept of the major components of an ECR-driven plasma source. The role of the individual components is discussed elsewhere [Roth 1995]. Redrawn from [Roth 1995].

Apart from the microwave power supply and control, determinant factors for the properties of the generated ECR plasmas are the magnetic configuration adopted and the vacuum chamber dimensions, which in the case of the microwave radiation are comparable with the corresponding wavelength (i.e.,  $\approx 12.23$  cm at 2.45 GHz) and in turn may raise impedance matching issues [Asmussen and Mak 1994]. In section 12.3, where existing negative ion sources are presented, different designs are demonstrated. Particularly, as regards the magnetic configuration, **Fig. 12.5** illustrates typical multipolar magnetic field cusp configurations, which can reduce wall losses and increase plasma density. In **Fig. 12.5(a)** a picket fence multipolar cusp is generated by a series of current-carrying wires on the outside of a vacuum vessel wall [Roth 1995]. Adjacent conductors have equal currents flowing in opposite directions. The same configuration can also be generated (and usually is) by a row of permanent magnets.

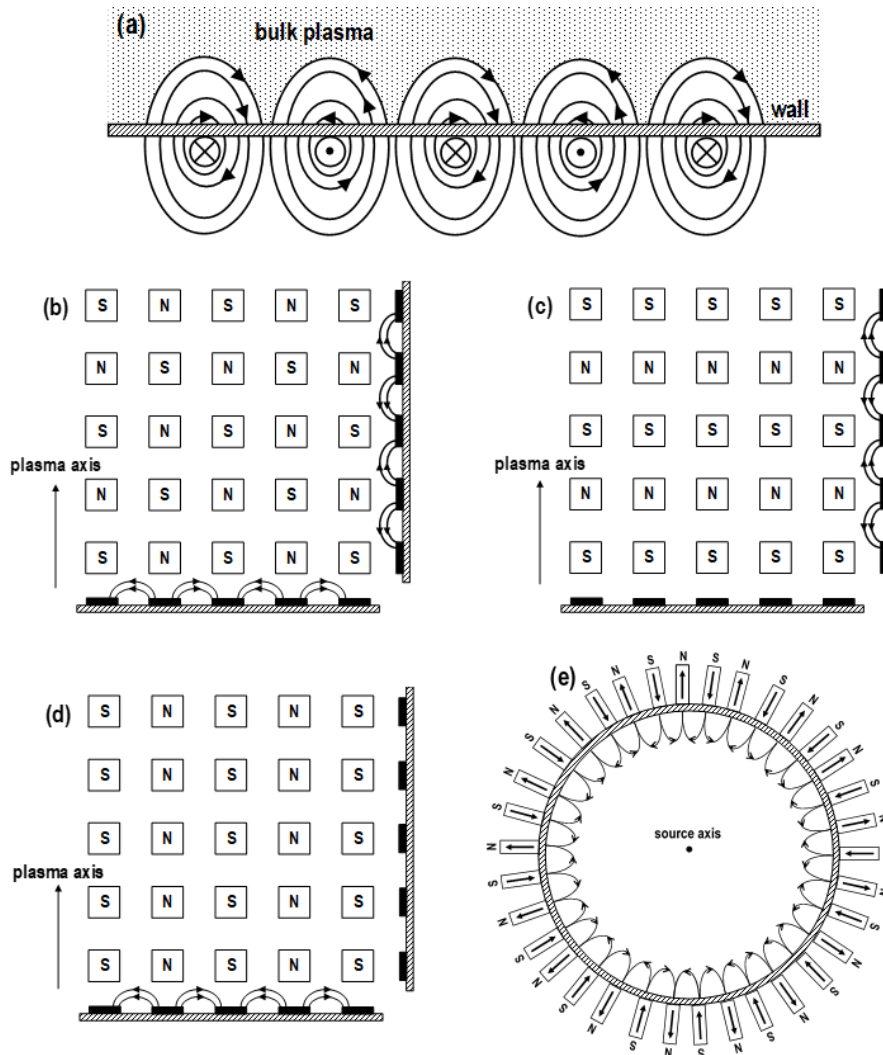


**Figure 12.5.** Different magnetic field configurations: (a) picket fence multipolar magnetic field; (b) checkerboard array; (c) axisymmetric cusp array; (d) longitudinal cusp array; (e) longitudinal cusp array multipolar magnets for confinement of cylindrical microwave plasmas. Redrawn from [Roth 1995].

The confined plasma will be kept away from the vessel wall by the increasing magnetic field, with some particles lost along the line cusp which contacts the wall halfway between the conductors [Roth 1995]. In the case of volume production negative ion sources, the negative ion yield is benefited by the trapping of high energy electrons in the magnetic field lines, as it is discussed later. It is usual practice to put water cooling lines outside the vacuum vessel halfway between the conductors, where cusp deposits the plasma constituents with their accompanying heat load.

Multipolar cusp confinement can be designed by small permanent magnets too, and **Figs. 12.5(b) – (d)** shows four different ways [Roth 1995]. **Fig. 12.5(b)** shows the checkerboard array which produces cusps both axially and

azimuthally, with the plasma axis pointing upward. **Fig. 12.5(c)** is an axisymmetric cusp array which gives a series of axisymmetric cusps along the axial length of the vacuum vessel wall. In **Fig. 12.5(d)** is the longitudinal cusp array, which gives a series of longitudinal cusps which vary in azimuth as one moves around the circumference of the vessel, but with little or no axial variation. Finally, **Fig. 12.5(e)** refers to a longitudinal cusp array, where the multipolar cusp confinement is achieved by parallel rows of permanent magnets located on the exterior periphery of the cylindrical portion of the vacuum chamber.

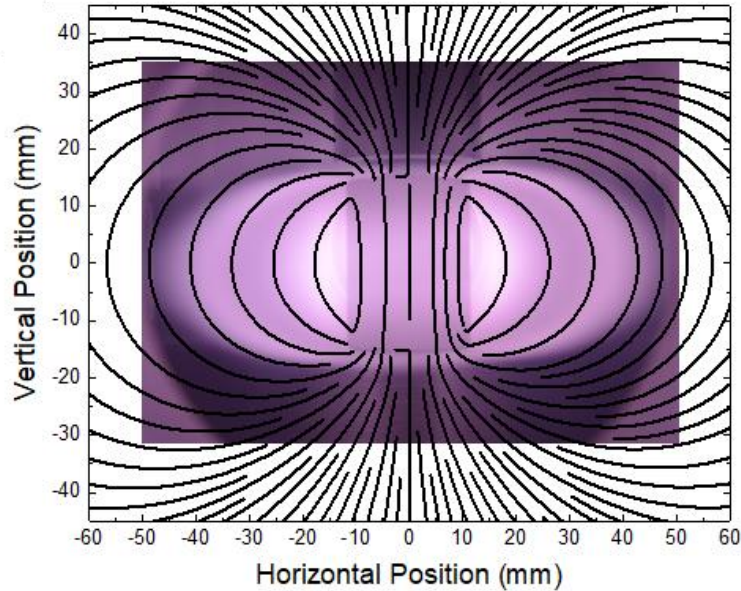


**Figure 12.6.** ECR plasma elementary module, operating at low pressure hydrogen plasma [Aleiferis *et al.* 2018]. The encapsulated permanent magnet is here surrounded by the ECR zone and the opening of the microwave applicator on its rear pole is distinguished. The pattern of the streamlines of the simulated magnetic field is superimposed.

A special design of ECR configuration is shown in **Fig. 12.6**. In this case the magnetic fields are not adjacent to the vessel walls as in **Fig. 12.5**. The design for each elementary plasma source is based on multi dipolar plasma principles [Lacoste *et al.* 2002]. The plasma source is made up of two main parts, i.e., a permanent magnet with an azimuthal symmetry around its magnetization axis, and a microwave applicator constituted by a coaxial line, parallel to the magnetization vector, and open on the rear pole of the magnet. In the design proposed in **Fig. 12.6**, the inner conductor of the coaxial line penetrates inside the cylindrical magnet through a hole drilled on its axis. The magnets are completely encapsulated in a metallic (stainless steel) envelope and water-cooled by using the inner tube inside the magnet. The microwave power can thus be transmitted without loss to the region of ECR coupling in front of the rear pole of the magnet with the help of a coaxial line: there is no possibility for microwaves to be absorbed by the plasma before reaching the ECR coupling region or to radiate towards an adjacent elementary source. Therefore, there is no possibility of interference between the elementary sources. In addition, as these elementary sources are at the ground potential, arcing does not appear between them and the reactor walls. Therefore, large size uniform plasmas can be obtained by assembling as many elementary plasma sources as necessary in a two-dimensional network. These elementary plasma sources can be assembled in different ways, e.g., networks of elementary plasma sources with alternate or identical magnetic polarities, rectangular or hexagonal networks, or other combinations.

## 12.2 H<sup>-</sup> and D<sup>-</sup> Negative Ion Production and Destruction Processes in ECR-driven Plasmas

The development of modern negative ion sources started in the 70s with the discovery of two important negative ion formation processes, namely [Bacal 2006; Bacal *et al.* 2021]: (i) surface production and (ii) volume production. The first process refers to the so-called resonant tunneling ionization and this is based on anion formation on low work function surfaces, which are typically metals covered by a (sub-micro)layer of an alkali element (e.g. cesium). The second process is mainly due to dissociative electron attachment (DA) of low energy electrons to (ro)vibrationally excited molecules.

Although the two processes may coexist in a negative ion source, the first dominates in cesiated sources and the second in cesium-free, volume production sources. The design of the negative ion sources operating with molecular hydrogen ( $H_2$ ) or deuterium ( $D_2$ ) to yield the corresponding ions ( $H^-$  or  $D^-$ ) has been extensively based on both concepts (surface and volume production). Reviews of this task can be found in the literature [Bacal and Wada 2015; Bacal and Wada 2020]. That said, regarding the available ECR-driven sources, they are mostly based on the volume production mechanisms. Various  $H^-$  or  $D^-$  ion production and destruction paths are possible in volume production sources. **Table 12.1** summarizes some of them and the principal ones are grey-highlighted.

**Table 12.1:** Tabulation of main reactions for the volume production and destruction of  $H^-$  negative ions. Principal ones are grey-highlighted. Equivalent reactions are valid in the case of  $D^-$  negative ions.

<b>PRODUCTION</b>		
$e + H_2(X^1\Sigma_g^+;v) \rightarrow H_2 \rightarrow H + H^-$	Dissociative Electron Attachment: DEA	[Bardsley <i>et al.</i> 1979; Celiberto <i>et al.</i> 2001]
$e + H_2^+ \rightarrow H^+ + H^-$	Dissociative Recombination: DR	[Bacal and Wada 2020; Peart <i>et al.</i> 1973]
$e + H_3^+ \rightarrow H_2^+ + H^-$	Dissociative Recombination: DR	[Bardsley and Wadehra 1979]
$e + H_2(v,J) \rightarrow H^- + H^+ + e$	Polar Dissociation	[Bardsley and Wadehra 1979]
$H_2 + H_2^+ \rightarrow H^- + H + 2H^+$	Ion-Molecule Collisions	[Bardsley and Wadehra 1979] (by analogy
$H_2 + H_2^+ \rightarrow H^- + H^+ + H_2^+$		with reactions in $D_2$ )
<b>DESTRUCTION</b>		
$H^- + H \rightarrow H_2 + e$	Associative Detachment: AD	[Miller 2012]
$H^- + H \rightarrow H_2(v) + e$	Associative Detachment (AD) with creation of vibrationally excited molecules	[Graham 1995]
$H^- + H \rightarrow 2H + e$	non-Associative Detachment: non-AD	[Javen <i>et al.</i> 2003]
$H^- + e \rightarrow H + 2e$	Electron Detachment: ED	[Javen <i>et al.</i> 2003]
$H^- + H_2(v) \rightarrow H_2(v-2) + H + e, 2 \leq v \leq 6$	Electron Detachment in collisions with vibrationally excited molecules: EDV	[Yang <i>et al.</i> 2018; Dem'yanov <i>et al.</i> 1985]
$H^- + H_2 \rightarrow H_2 + H + e$	Collisional Detachment: CD	[Huq <i>et al.</i> 1983]
$H^- + H^+ \rightarrow 2H$	Mutual Neutralization: MN	[Yang <i>et al.</i> 2018; Eerden <i>et al.</i> 1995]
$H^- + H^+ \rightarrow H + H(n=2, 3)$		[Yang <i>et al.</i> 2018; Matveyen & Silakov 1995]
$H^- + H_2^+ \rightarrow H_2 + H$		[Yang <i>et al.</i> 2018; Matveyen & Silakov 1995]
$H^- + H_2^+ \rightarrow 3H$		[Yang <i>et al.</i> 2018; Eerden <i>et al.</i> 1995]
$H^- + H_2^+ \rightarrow H + H_2(v)$		[Graham <i>et al.</i> 1995]
$H^- + H_3^+ \rightarrow 2H_2$		[Yang <i>et al.</i> 2018, Matveyen & Silakov 1995]
$H^- + H_3^+ \rightarrow 4H$		[Yang <i>et al.</i> 2018; Eerden <i>et al.</i> 1995]
$H^- + H_3^+ \rightarrow 2H + H_2(v)$		[Graham <i>et al.</i> 1995]

Regarding the main production path, i.e., DEA, **Fig. 12.7** shows the associated cross-section. In both  $H_2$  and  $D_2$  gases, the cross sections peak at relative low energy electrons, whereas it increases for diminishing energy. Such low energy electrons are readily produced in the ECR sources as part of bi-Maxwellian electron energy distribution functions (EEDFs), as it will be discussed below in case studies.

On the other hand, DEA reaction necessitates the existence of (ro)vibrationally excited molecules. **Table 12.2** presents the (de)excitation paths of these molecules and the dominant ones are grey-highlighted. Vibrational excitation of molecules in collisions with low energy electrons (eV excitation) is effective in changing the vibrational state [Capitelli *et al.* 2006], but the most probable change in  $v$  is  $\Delta v = \pm 1$  [Bacal 2006]. A high collision rate or low vibrational de-excitation rate would thus be required to significantly populate the spectrum. In addition, apart from this change of vibrational level by one, eV excitation results in equilibrium of lower vibrational levels [Capitelli *et al.* 2006; Mosbach 2005].

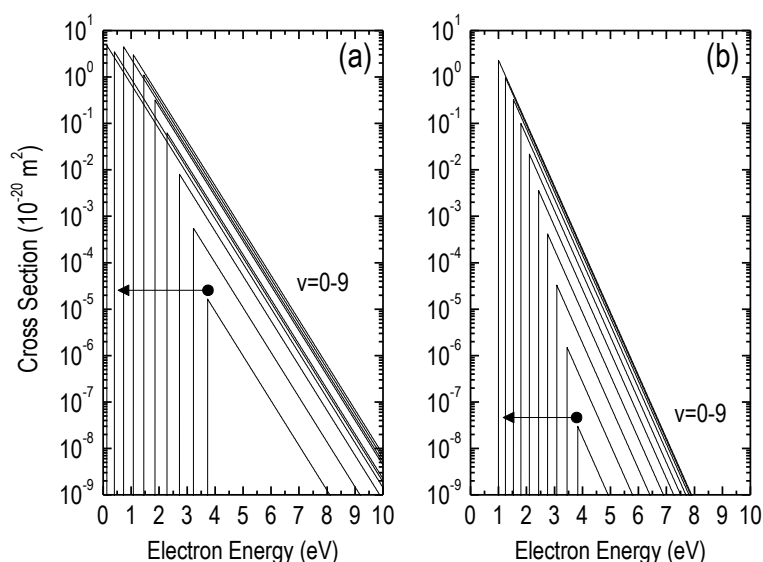
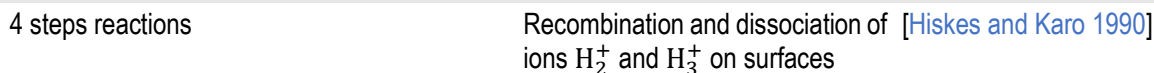


**Figure 12.7.** Cross section of the DEA reactions in the case of (a)  $H_2$  and (b)  $D_2$ . The curves are plotted according to the available data Tables in Ref. [Celiberto *et al.* 2001].

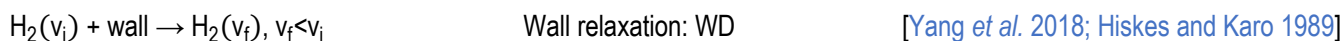
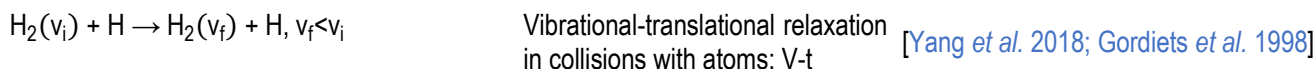
Conversely, the predominant channel for the formation of highly vibrationally excited molecules is related to excitation to singlet electronic states followed by spontaneous emission (EV excitation) [Hiskes 1980]. The cross sections involved in the EV excitation, both in  $H_2$  and  $D_2$ , are given in Fig. 12.8, while Franck-Condon factors are presented elsewhere [Fantz and Wunderlich 2006]. High energy electrons are a prerequisite for excitation. Thus, while DEA entails low energy electrons, at the same time it implies the need for high electron electrons since (ro)vibrationally excited molecules are precursors of the reaction itself. As it will be discussed below, ECR plasmas are capable of providing such dual populations (i.e., cold, and hot) in a spatially resolved manner.

**Table 12.2:** Tabulation of main reactions for the population and de-excitation of vibrational states in  $H_2$ . Principal ones, discussed in this chapter, are grey-highlighted. Equivalent reactions are valid in the case of  $D_2$  ions.

#### EXCITATION



#### DE-EXCITATION



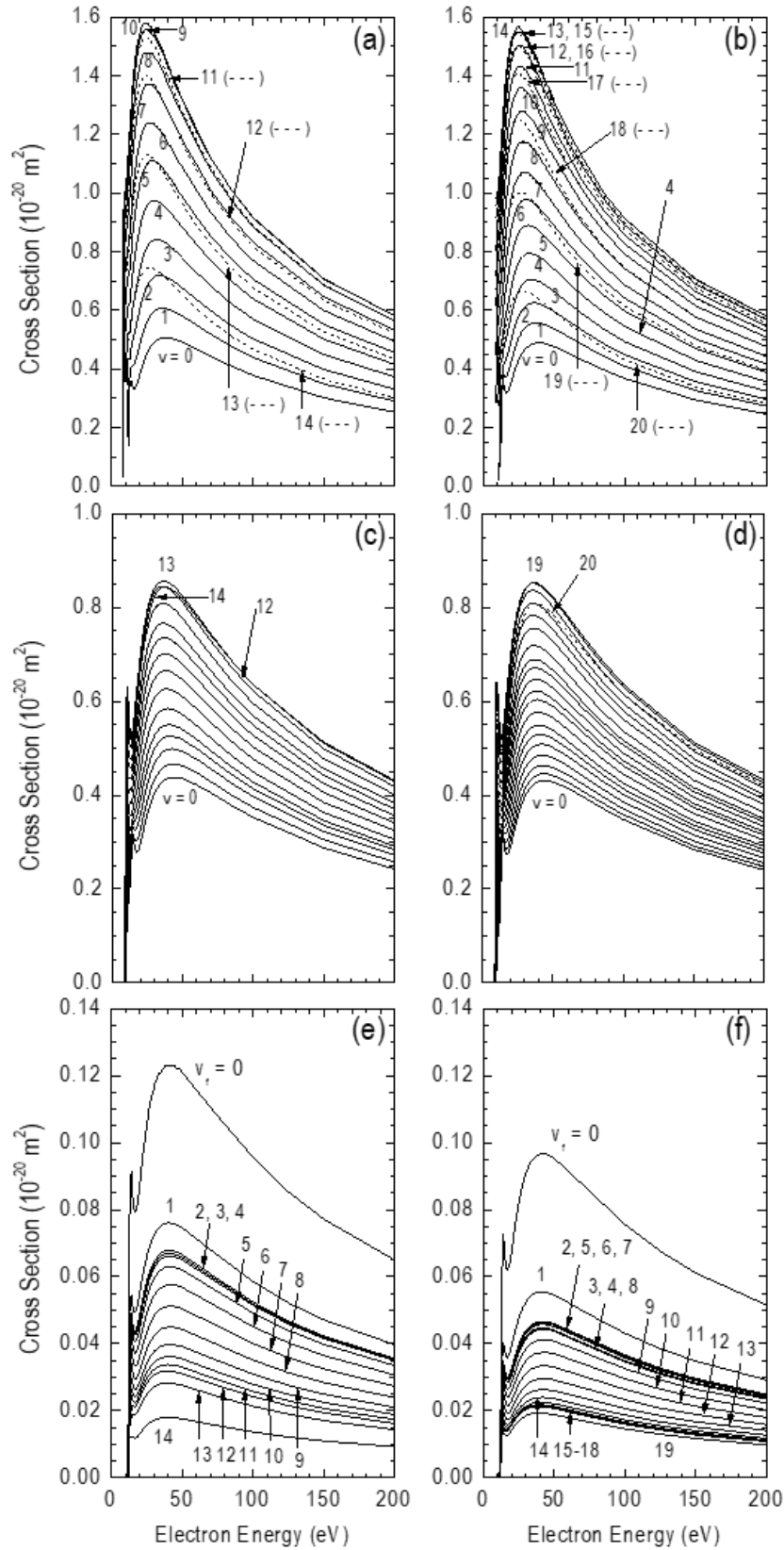


**Figure 12.8:** Cross sections related to the EV process: **(a)**  $\text{H}_2(X^1\Sigma_g^+; v_i) + e \rightarrow \text{H}_2(B^1\Sigma_u^+) + e$ ; **(b)**  $\text{D}_2(X^1\Sigma_g^+; v_i) + e \rightarrow \text{D}_2(B^1\Sigma_u^+) + e$ ; **(c)**  $\text{H}_2(X^1\Sigma_g^+; v_i) + e \rightarrow \text{H}_2(C^1\Pi_u) + e$ ; **(d)**  $\text{D}_2(X^1\Sigma_g^+; v_i) + e \rightarrow \text{D}_2(C^1\Pi_u) + e$ ; **(e)**  $\text{H}_2(X^1\Sigma_g^+; v_i) + e \rightarrow \text{H}_2(B^1\Sigma_u^+, C^1\Pi_u) + e \rightarrow \text{H}_2(X^1\Sigma_g^+; v_f) + e + h\nu, v_f > v_i = 0$ ; **(f)**  $\text{D}_2(X^1\Sigma_g^+; v_i) + e \rightarrow \text{D}_2(B^1\Sigma_u^+, C^1\Pi_u) + e \rightarrow \text{D}_2(X^1\Sigma_g^+; v_f) + e + h\nu, v_f > v_i = 0$ . The curves are plotted according to the available data Tables in Ref. [Celiberto et al. 2001].

A challenging effect relative to volume production is the formation of the  $H_2$  and  $D_2$  excited molecules through wall processes, instead of reactions in the bulk plasma. Two vibrational excitation processes have been identified: (i) production of vibrationally excited molecules due to the recombination of molecular hydrogen ions on the walls [Hiskes & Karo 1990], and (ii) production of a wide spectrum of rovibrationally excited molecules in the recombinative desorption process of atomic hydrogen on some metal surfaces [Hall *et al.* 1988]. The surface recombination mechanisms can be of three generic types [Kolasinski 2019]: (i) Langmuir-Hinshelwood (thermal diffusion of two adsorbates) [Baxter and Hu 2002] and, more importantly in terms of energy deposition into the formed molecules, (ii) Eley-Rideal (direct impact of an atom from the plasma with an adsorbate) [Eley and Rideal 1940], and (iii) hot-atom reactions (indirect collision consisting of several encounters with the surface and adsorbates) [Kammler *et al.* 2000]. The hot-atom reactions replace in some cases the Eley-Rideal mechanism when a gas-phase atom incident on a surface combines with a particle adsorbed onto that surface. ECR-based experiments designed for exploiting these mechanisms are illustrated in the next section.

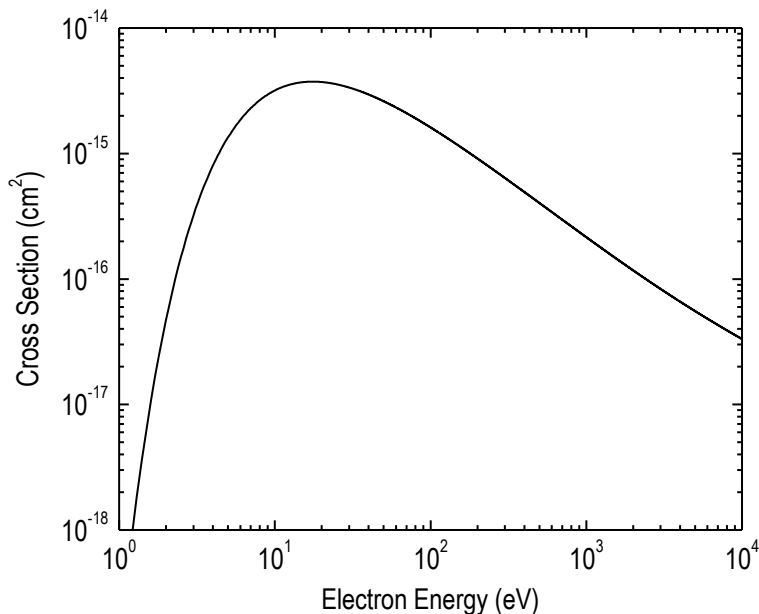


**Figure 12.9.** Cross section of the electron detachment (ED) reaction in hydrogen, according to analytic fit equation [Janev *et al.* 2003].

Instead, **Fig. 12.9** presents the cross section of one of the main destruction reactions (**Table 12.1**), i.e., electron detachment (ED). Considering the above discussion on the necessity of high energy electrons to produce excited molecules, which in turn lead to negative ion production in volume sources, and the fact that ED becomes more probable when electrons of similar energies (i.e., around 20 eV) are present, it is evident that a complicated balance between various species should be considered to unfold the physics of volume sources. In the next sections, case studies of operating ECR sources are given, supporting all the statements and concepts analyzed by now. Finally, it is underlined that the volumetric rates of both the production and destruction processes depend strongly on the electron energy distribution functions.

### 12.3 Representative $H^-$ and $D^-$ Negative Ion Sources

In this section, following the aforementioned presentation on the ECR heating concept and the reactions that rule the negative ion volume production, representative ECR-driven sources that have provided numerous experimental results are considered. Different designs and a wide variety of operational windows, are discussed. Selected results are reviewed and analyzed, unveiling the main features and the capacity of the ECR volume sources.

Such results have been obtained by means of various tailored diagnostics. In general, the diagnostics employed for the plasma interrogation with respect to the ECR source principles, refer both to the charged species and excited neutral probing. Thus, principal techniques include: (i) Electrostatic probes for measurements on the plasma potential, plasma density, electron temperature and EEDFs [Godyak and Deminov 2011]; (ii) Laser induced photo-detachment for

measurements on the negative ion  $H^-$  and  $D^-$  density [Bacal 2000]; (iii) Optical emission spectroscopy for recording atomic and molecular transitions, and thus relative densities of neutral species (e.g., degree of dissociation) [Fantz 2006]; (iv) VUV spectroscopy for accessing to molecular plasma processes, including volumetric rates of ionization, dissociation and excitation to high vibrational levels and metastable states [Komppula *et al.* 2015]; (v) Laser induced fluorescence spectroscopy to measure the densities of rovibronically excited molecules [Mosbach 2005]; (vi) VUV Fourier transformer absorption spectroscopy based on synchrotron radiation for direct measurements of electronic ground state ro-vibrationally excited molecules in ECR plasmas [Béchu *et al.* 2020].

### 12.3.1 Camembert III

The source Camembert III is a large volume negative ion source, driven at 2.45 GHz microwave power. It is composed of three main elements: (i) A magnetic multipole chamber [Courteille *et al.* 1995], having a configuration like that shown in **Fig. 12.5.e**. Briefly, the sidewall of the cylindrical stainless-steel chamber is 44.0 cm in diameter and 45.0 cm in high. Sixteen columns of samarium-cobalt magnets (3.5 kG on their surface) are installed with the “N” and the “S” poles alternatively facing the plasma. These magnets are contained in water cooled stainless-steel tubes ( $\varnothing 2.6$  cm) welded to the internal surface of the source to allow steady state, high power discharge operation. The plasma diameter is therefore 38.8 cm (approximately). The end plates are not magnetized. One end of the chamber is bounded, in part, by the stainless-steel plasma electrode (PE) of the extractor ( $\varnothing 10$  cm), which contains an extraction hole of  $\varnothing 0.8$  cm, and in part by a water-cooled annular copper plate. This plate is connected to the plasma chamber sidewall, which is grounded. The neighboring plasma is magnetized and due to this and to a small positive bias of the plasma electrode, large densities of volume produced negative ions concentrate in this region. This fact is illustrated by the experimental results below. (ii) A two-dimension network of seven elementary independent plasma sources like those of **Fig. 12.6**. The network is installed on the top flange of the source. Six of the seven modules form an imaginary circle and are mounted on its circumference (per 60 degrees) in such a way that “N” poles face the plasma, whereas the seventh module is mounted in the center of the circle with its “S” pole facing the plasma. (iii) An ion- and electron-extraction system of four electrodes [Bacal *et al.* 1985], including the first electrode which is in contact with the plasma, as mentioned above.

Due to this configuration, three regions may be distinguished. (i) A driven region, which is located near the network of the seven elementary ECR sources and, possibly, on the periphery of the chamber within the strong multi-cusp magnetic field. In this region, the plasma is produced by the electrons accelerated in the ECR coupling area due to the microwave electric field applied via the coaxial lines (**Fig. 12.6**). These fast-hot electrons oscillate within two field lines and two mirror points in front of the opposite poles of the magnet, and drift azimuthally around the magnet acting as a tri-dimensional magnetron structure. The EEDFs can be assumed to be the sum of this hot electron population and another cold electron population, with Maxwellian distribution functions (see Section 12.3.2). The plasma produced by the inelastic collisions of the hot electrons along their itinerary then diffuses away from each magnet. The hot electrons remain trapped in the magnetic field, whereas the excited molecules and the cold population of electrons diffuses away from the magnetic field under the influence of density gradients and the resulting space charge electric field [Lagarde *et al.* 2001]. (ii) A production region, which extends over the central magnetic field free region. Here, the diffused excited molecules and the cold electrons lead to enhanced DEA process. Lastly, (iii) a near-extractor region, where a weakly magnetized region is bounded by the plasma electrode. This magnetic field is the stray magnetic field originating in the rear of the magnets located within the extractor. Its maximum value is 20 G at 10 mm above the plasma electrode surface.

**Fig. 12.10** provides values of the main plasma parameters as a function of the working pressure during the source operation with hydrogen (0.9 kW). The main part of the plasma density refers to cold electrons. Densities up to about  $3 \times 10^{10} \text{ cm}^{-3}$  are achieved in the production region (ii). At the same time, the electron temperature lies within the range demanded for efficient DEA (compare **Figs. 12.7a** and **12.10a**).  $H^-$  ion densities up to about  $1.5 \times 10^9 \text{ cm}^{-3}$  are yielded. The latter passes through a maximum at around 0.6 Pa and this has been correlated with the loss of vibrationally excited species due to VT process [Svarnas *et al.* 2006].

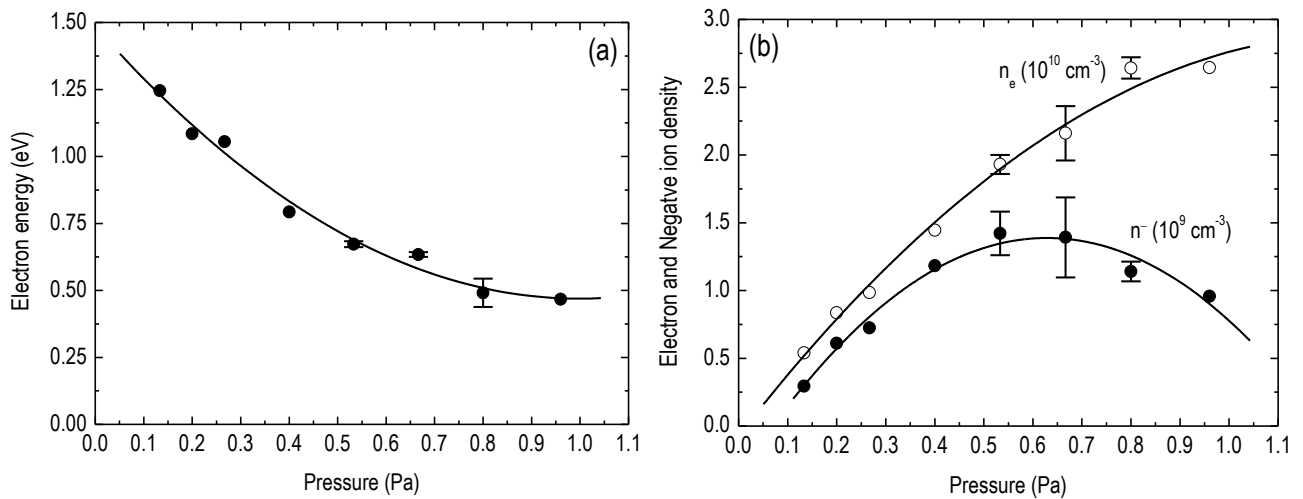


**Figure 12.10.** Basic plasma parameters, as a function of the operating hydrogen pressure, in the source Camembert III. (a) Cold electron energy. (b) Cold electron density ( $\circ$ ); Negative ion  $\text{H}^-$  density ( $\bullet$ ). Redrawn from [Svamas *et al.* 2006].

In this source, the weakly magnetized region (iii) has been studied extensively by varying the plasma electrode bias and observing the resultant effects on the local plasma parameters and the extracted currents [Svamas *et al.* 2007]. It is seen (Fig. 12.11a) that, the plasma electrode current increases monotonously versus the plasma electrode potential. An optimization of the source appears possible for bias values slightly higher (typically 1 V) than the local plasma potential (typically 4 V to 6 V). At that point, the extracted electron current decreases sharply and the extracted  $\text{H}^-$  ion current peaks. The correlation of this peak with the plasma parameters measured in region (iii) is illustrated in Fig. 12.11b. In this figure, the electron-to-negative ion density ratio matches the electron-to-negative ion extracted current ratio for variable plasma electrode bias.

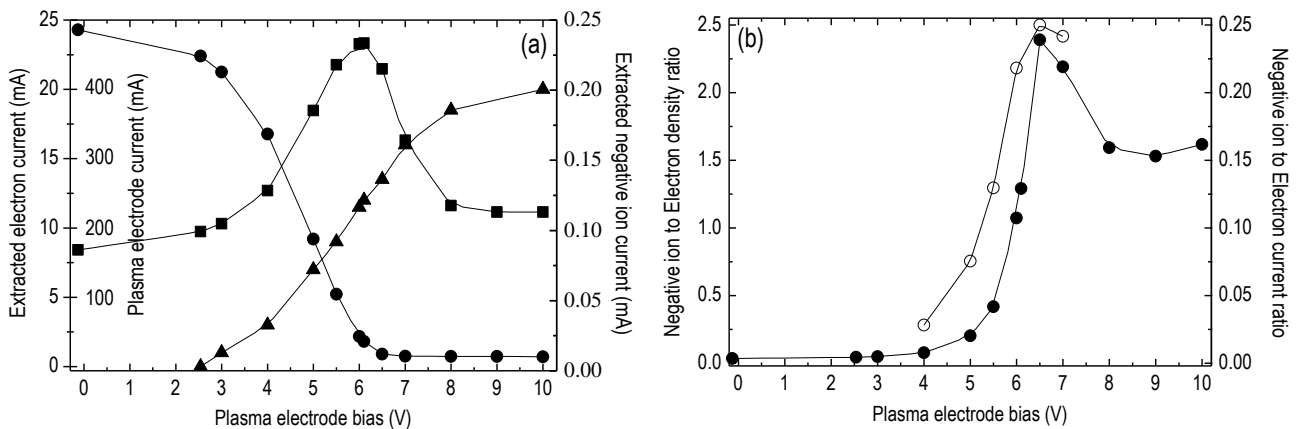


**Figure 12.11.** Dependence on the plasma electrode bias of the: (a) plasma electrode current ( $\blacktriangle$ ); extracted electron current ( $\bullet$ ); extracted negative ion current ( $\blacksquare$ ), 0.27 Pa; (b) ratio of the negative ion to electron densities ( $\circ$ ); ratio of the negative ion to electron extracted currents ( $\bullet$ ), 0.27 Pa, 0.75 cm above PE. Redrawn from [Svamas *et al.* 2007].

In more detail [Svamas *et al.* 2007]: the decrease in the extracted electron current is the result of the depletion of the electron population by the positively biased plasma electrode. The weak magnetic field in front of this electrode prevents the replacement of these depleted electrons by new electrons arriving from the bulk plasma. This disturbs the local plasma neutrality and thus other negatively charged species should replace the depleted electrons. Therefore, volume produced  $\text{H}^-$  negative ions, originating in the production region (ii), arrive within the magnetized region over the positively biased plasma electrode. As far as the bias level breaks the local plasma potential, the  $\text{H}^-$  ions are no longer electrostatically trapped and can thus be extracted. The maximum extraction is obtained at about 1 V above the plasma potential. When the bias increases further, the volume produced  $\text{H}^-$  ions are accelerated towards the plasma electrode

and the  $H^-$  ion speed increases over the plasma electrode. The  $H^-$  ion residence time decreases due to the larger speed and the  $H^-$  ion density goes down. Eventually,  $H^-$  ions can be collected by the plasma electrode.

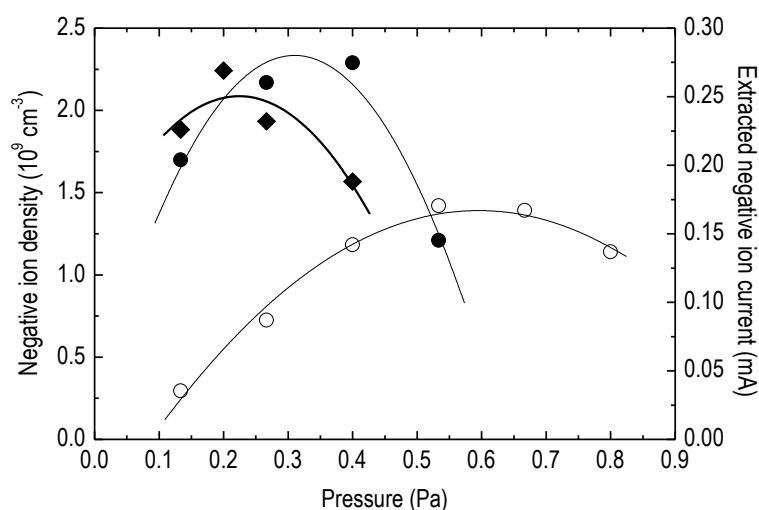


**Figure 12.12.** Correlation between the negative ion density and the corresponding extracted current, for variable operating pressure in hydrogen.  $H^-$  negative ion density 15 cm ( $\circ$ ) and 0.75 cm ( $\bullet$ ) above the plasma electrode surface, and extracted negative ion current ( $\blacklozenge$ ). Redrawn from [Svarnas *et al.* 2007].

**Fig. 12.12** compares directly the  $H^-$  ion densities between the regions (ii) (15 cm above the plasma electrode) and (iii) (0.75 cm above the plasma electrode) and the corresponding extracted current, over the entire range of the operating pressure. Two points are stressed. Firstly, the  $H^-$  ion extracted current can only be correlated with the related  $H^-$  ion density close to the extraction aperture and not with the one yielded far away from this. Secondly, the above described role of the stray magnetic field over the extraction aperture is critical, since it leads to enhanced negative ion-to-electron density ratios, as compared to the values obtained at longer distances where this magnetic field is negligible.

### 12.3.2 Prometheus I

The source Prometheus I [Aleiferis *et al.* 2016; Aleiferis *et al.* 2018] consists of a cubic (240 mm inner edge) stainless steel chamber with the necessary viewports for plasma diagnostics. The plasma is sustained by a 2D network of five ECR plasma elementary sources like those shown in **Fig. 12.6**. Four sources are installed at the vertices and the fifth at the center of an imaginary square (160 mm side length) on the top flange of the high vacuum chamber. The four permanent magnets face the plasma with their “S” poles and the fifth with its “N” pole. Each elementary source is driven by an independent microwave solid-state power supply (2.45 GHz) able to provide up to 180 W. A tuner embedded on the main body of each source, is used for the impedance matching which maximizes the microwave power absorbed by the plasma. The elementary sources and their power supplies are cooled by water which is circulated by a closed system. The source operates either with hydrogen ( $H_2$ ) or deuterium ( $D_2$ ), within a pressure range between 0.13 and 2.67 Pa.

**Fig. 12.13** shows that two electronic populations are produced due to ECR heating, a “cold” and a “hot” one, having about one order of magnitude difference in their temperatures. At the same time, **Fig. 12.14** gives the absolute density values of these populations, unveiling a difference of about two orders of magnitude in favor of the cold population. These measurements are carried out 65 mm downstream of the ECR zone middle planes [Mitrou *et al.* 2021]. The hot population downstream of the ECR zones is a fingerprint of the energetic electrons generated in these zones, whereas the cold population refers to the electrons escaping these zones [Lagarde *et al.* 2001]. The former promotes ro-vibrational excitation of molecules (EV reaction) which eventually diffuse away from the heating zones. The latter promote  $H^-$  and  $D^-$  ion production through the dissociative attachment (DA) reaction, between them and the diffused excited molecules, in the source volume. The densities of both populations tend progressively to a quasi saturation as the gas pressure increases.

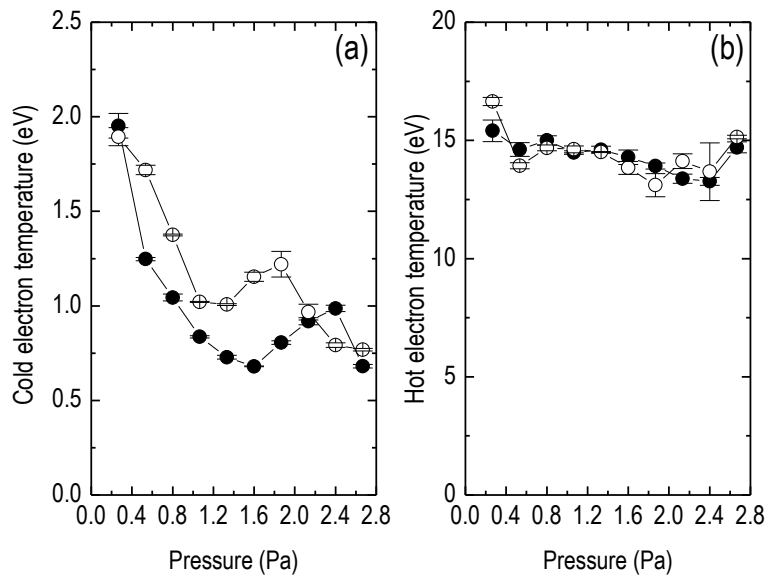


**Figure 12.13.** (a) Cold and (b) hot electron temperature versus the operating gas pressure [Mitrou *et al.* 2021]. ● H<sub>2</sub>; ○ D<sub>2</sub>; 0.9 kW.

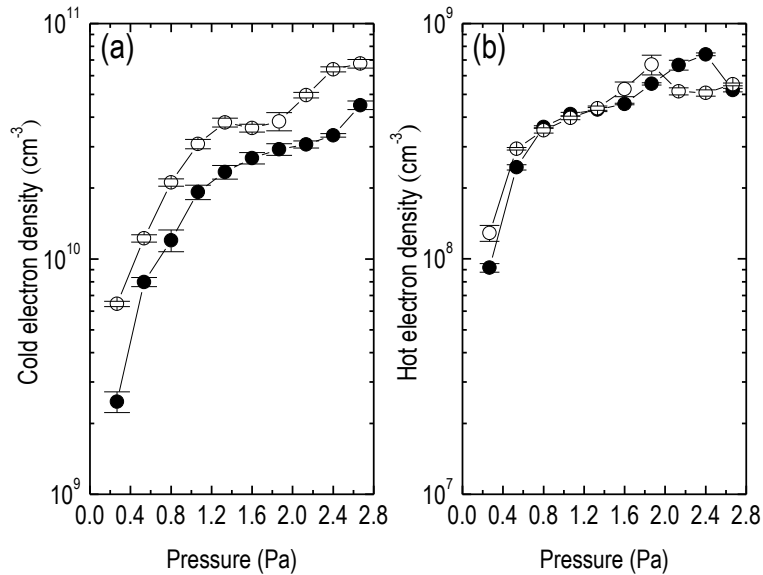


**Figure 12.14.** (a) Cold and (b) hot electron density versus the operating gas pressure [Mitrou *et al.* 2021]. ● H<sub>2</sub>; ○ D<sub>2</sub>; 0.9 kW.

On the other hand, **Fig. 12.15(a)** makes a direct comparison between the negative ion yields achieved in the two gases [Mitrou *et al.* 2021]. At a first glance, H<sup>-</sup> and D<sup>-</sup> densities have a qualitatively and quantitatively similar evolution as a function of the operating pressure, i.e., a sharp increase is followed by a quasi saturated phase. Despite that, an obvious isotope effect is exhibited by a different presentation of the data. In **Fig. 12.15(b)** the relative negative ion density is given, unveiling a strong isotope effect in support of the H<sup>-</sup> ions and a sharp optimum around 1.33 Pa in both gases [Mitrou *et al.* 2021]. On the top of that, **Fig. 12.16(a)** compares the promote H<sup>-</sup> and D<sup>-</sup> densities under equal plasma density (cold electrons), following pressure elimination [Mitrou *et al.* 2021]. Higher values for the H<sup>-</sup> ion density, are observed. The corresponding curves versus the hot electrons (**Fig. 12.16(b)**) are associated with closer experimental points in the two gases.

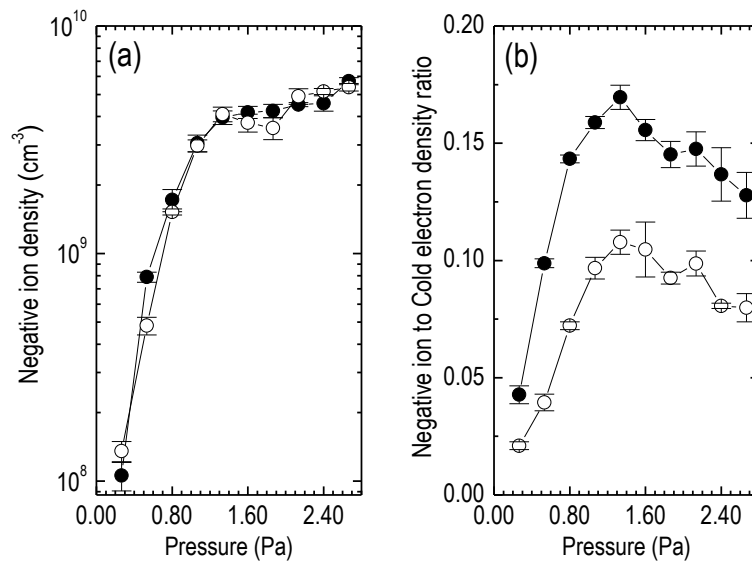


**Figure 12.15:** (a) H<sup>-</sup> and D<sup>-</sup> ion density and (b) H<sup>-</sup> and D<sup>-</sup> ion to cold electron density ratio, versus the operating gas pressure [Mitrou *et al.* 2021]. ● H<sub>2</sub>; ○ D<sub>2</sub>; 0.9 kW.

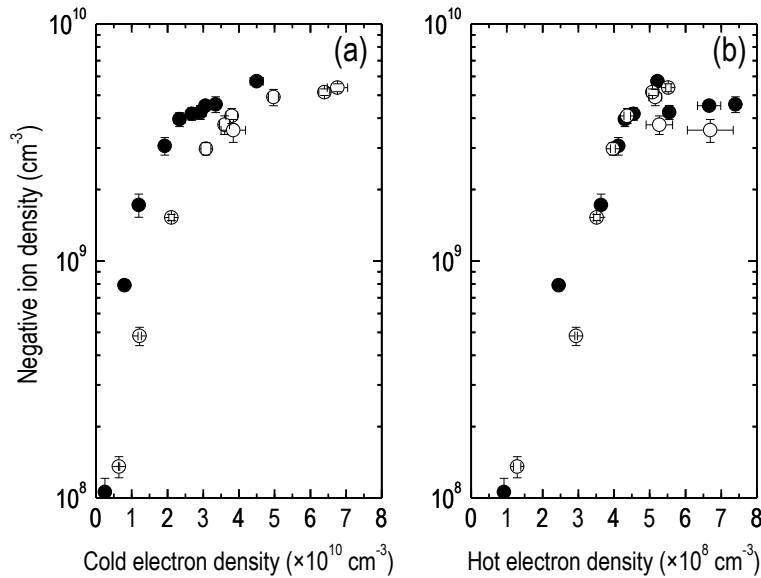


**Figure 12.16.** H<sup>-</sup> and D<sup>-</sup> ion density versus (a) cold and (b) hot electron density. Data pairs are created with the pressure elimination [Mitrou *et al.* 2021]. ● H<sub>2</sub>; ○ D<sub>2</sub>; 0.9 kW.

Further insight into this source operation has been achieved by varying the microwave power injected by the five ECR modules, up to 0.9 kW, for three different pressures (0.53, 1.07, and 1.60 Pa). Regarding the plasma potential, higher values are measured, in both H<sub>2</sub> and D<sub>2</sub> gases, as the power increases and the pressure decreases. However, it appears higher (up to about 2 V) in the case of D<sub>2</sub> gas, independently of the pressure and the power. Then, similar to the results of Fig. 12.13(a), deuterium is associated with higher cold electron energies than hydrogen does, and this energy increases in a non-monotonic way versus the power. Regarding hot electron population, values between 14 and 16 eV are constantly recorded, as in Fig. 12.13(b). On the other hand, both cold and hot electron densities increase as a function of the microwave power, whereas D<sub>2</sub> yields higher densities of cold electrons. The difference on the hot electron density between the two gases is less pronounced. Representative data on these plasma parameters are tabulated below for facilitating the comparison.

**Table 12.3:** Key parameters of the ECR plasma in the source Prometheus I, when it works within different operational windows.

	0.53 Pa		1.07 Pa		1.60 Pa	
0.15 kW	H <sub>2</sub>	D <sub>2</sub>	H <sub>2</sub>	D <sub>2</sub>	H <sub>2</sub>	D <sub>2</sub>
V <sub>pl.</sub> (V)	5.47	6.64	5.37	6.62	5.05	6.54
T <sub>e</sub> <sup>cold</sup> (eV)	0.63	0.91	0.58	0.74	0.55	0.67
T <sub>e</sub> <sup>hot</sup> (eV)	10.72	14.12	13.92	15.19	14.39	15.16
n <sub>e</sub> <sup>cold</sup> (m <sup>-3</sup> )	1.62×10 <sup>15</sup>	2.65×10 <sup>15</sup>	2.96×10 <sup>15</sup>	4.56×10 <sup>15</sup>	3.29×10 <sup>15</sup>	5.98×10 <sup>15</sup>
n <sub>e</sub> <sup>hot</sup> (m <sup>-3</sup> )	5.29×10 <sup>13</sup>	5.66×10 <sup>13</sup>	9.73×10 <sup>13</sup>	1.05×10 <sup>14</sup>	1.12×10 <sup>14</sup>	1.19×10 <sup>14</sup>
0.5 kW	H <sub>2</sub>	D <sub>2</sub>	H <sub>2</sub>	D <sub>2</sub>	H <sub>2</sub>	D <sub>2</sub>
V <sub>pl.</sub> (V)	7.52	8.33	7.01	8.11	6.59	7.91
T <sub>e</sub> <sup>cold</sup> (eV)	0.91	1.53	0.72	0.96	0.57	0.82
T <sub>e</sub> <sup>hot</sup> (eV)	15.34	14.12	15.38	15.06	15.72	15.19
n <sub>e</sub> <sup>cold</sup> (m <sup>-3</sup> )	4.95×10 <sup>15</sup>	6.70×10 <sup>15</sup>	1.28×10 <sup>16</sup>	1.86×10 <sup>16</sup>	2.09×10 <sup>16</sup>	3.04×10 <sup>16</sup>
n <sub>e</sub> <sup>hot</sup> (m <sup>-3</sup> )	1.34×10 <sup>14</sup>	1.77×10 <sup>14</sup>	2.67×10 <sup>14</sup>	2.84×10 <sup>14</sup>	3.27×10 <sup>14</sup>	3.16×10 <sup>14</sup>
0.9 kW	H <sub>2</sub>	D <sub>2</sub>	H <sub>2</sub>	D <sub>2</sub>	H <sub>2</sub>	D <sub>2</sub>
V <sub>pl.</sub> (V)	8.11	10.13	7.72	9.06	7.03	8.49
T <sub>e</sub> <sup>cold</sup> (eV)	1.28	1.69	0.83	1.02	0.69	1.16
T <sub>e</sub> <sup>hot</sup> (eV)	15.11	14.31	15.13	14.71	15.01	13.54
n <sub>e</sub> <sup>cold</sup> (m <sup>-3</sup> )	7.06×10 <sup>15</sup>	1.39×10 <sup>16</sup>	1.91×10 <sup>16</sup>	3.29×10 <sup>16</sup>	2.82×10 <sup>16</sup>	3.51×10 <sup>16</sup>
n <sub>e</sub> <sup>hot</sup> (m <sup>-3</sup> )	2.29×10 <sup>14</sup>	2.79×10 <sup>14</sup>	3.82×10 <sup>14</sup>	3.92×10 <sup>14</sup>	4.36×10 <sup>14</sup>	5.33×10 <sup>14</sup>

Regarding the H<sup>-</sup> and D<sup>-</sup> ion yields, **Fig. 12.17** illustrates the density values as a function of the power at different working pressures. In general, the production efficiency in both gases seems comparable, but **Fig. 12.18** demonstrates an isotope effect similar to that of **Fig. 12.15(b)**. Thus, H<sub>2</sub> promotes higher relative negative ion density under all conditions and, additionally, an optimal operational window is revealed in both H<sub>2</sub> and D<sub>2</sub>. The latter corresponds to intermediate pressure and power levels. Finally, by eliminating the power and plotting the negative ion density versus the cold or hot electron density, the trends of **Fig. 12.16** are reproduced.

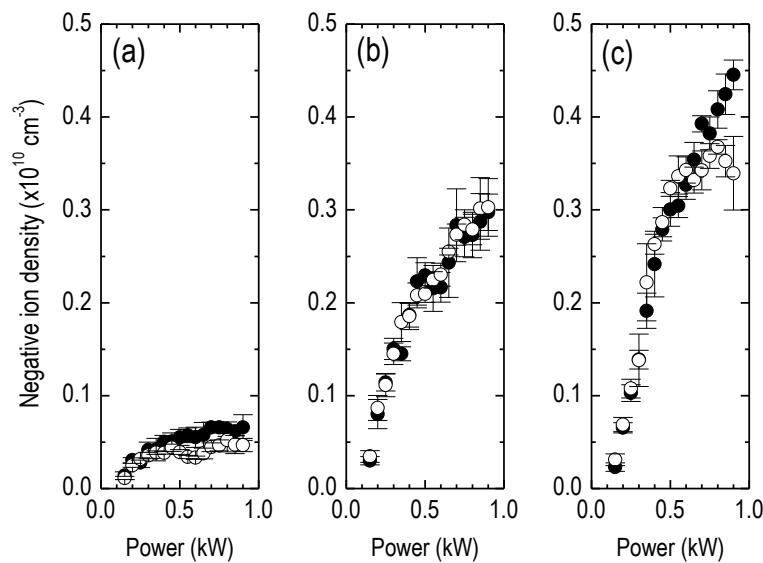


**Figure 12.17.** Negative ion density as a function of the microwave power at (a) 0.53 Pa, (b) 1.07 Pa, and (c) 1.60 Pa. Solid circles: H<sub>2</sub> plasma. Open circles: D<sub>2</sub> plasma.

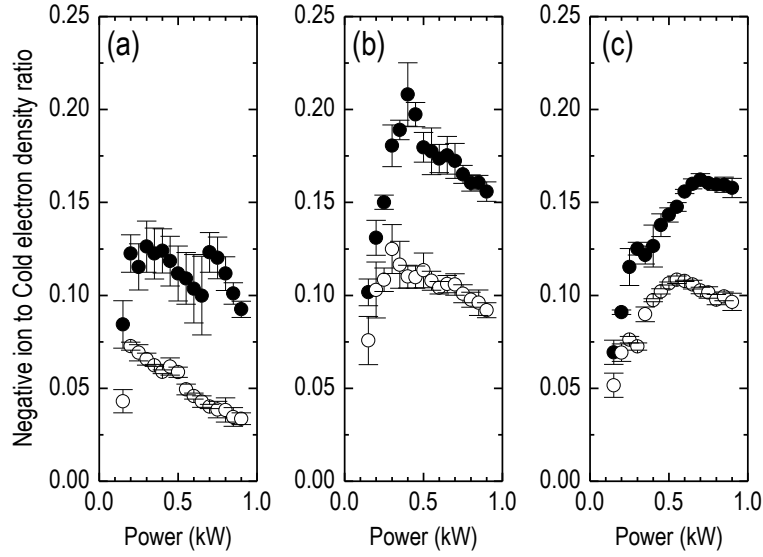


**Figure 12.18.** Negative ion to Cold electron density as a function of the microwave power at (a) 0.53 Pa, (b) 1.07 Pa, and (c) 1.60 Pa. Solid circles: H<sub>2</sub> plasma. Open circles: D<sub>2</sub> plasma.

### 12.3.3 ECR with driven plasma rings

An alternative type of ECR source with stratified plasma has been proposed by [Dougarg *et al.* 1992] as a good alternative for hydrogen negative ion production. In this source, a mechanism of electron heating in the resonance zones takes place and leads to ring structure creation. A radial ambipolar electric field emerging between the heating rings and the cold plasma results in azimuth drift rotation of these rings. It has been found [Dougarg *et al.* 1998] that the ring driven structure is a controlling factor for negative ion production.

The concept of the source is given Fig. 12.19 and details have been reported previously [Dougarg-Jabon *et al.* 1998; Dougarg-Jabon *et al.* 1992; Dougarg-Jabon 2001; Velasco *et al.* 2015]. Briefly, the discharge chamber comprises a 13 cm in diameter and 8 cm long aluminum cylinder, placed axisymmetrically between two identical Sm-Co magnetic poles with a surface magnetization of 1100 G. The magnets create a mirror trap. The magnetic field in the plasma volume is modified by the variation of the distance between the magnets, but its configuration remains of the mirror type. An oscillator of 2.45 GHz excites a microwave field of TE<sub>111</sub> mode in the chamber volume, whose electrical component is perpendicular to the static magnetic force lines. The fundamental resonance surface and the surfaces corresponding to the first three harmonics of the fundamental electron cyclotron frequency shape hyperboloids of one sheet, i.e.,

$$B_{cl,k}(r, z) = \frac{m c \omega}{e k} \quad \text{Eq. (9)}$$

where  $\omega$  stands for the microwave frequency and  $k = 1, 2, 3, 4$ . The fundamental resonance ( $k = 1$ ) is observed at the surface  $B_{cl,1}(r, z) = 845$  G which has a radius in the midplane of the magnetic trap equal to 1.6 cm (when the space between the poles is 8.9 cm), whereas the radii corresponding to the harmonics  $k = 2, 3$ , and 4 are 4.3, 5.1, and 6.1 cm, respectively.

Although ECR interaction takes place on the whole surface of the resonance hyperboloids, the energetic electrons are in a stable position only in the midplane of the mirror trap where they form a multiring structure. The cross section of these hyperboloids and the electron rings within the discharge are illustrated in Fig. 12.19. A radial ambipolar electric field emerging between the heated rings and the cold plasma results in azimuth drift rotation of these rings. Rotation speeds are ranged from about  $3 \times 10^7$  m s<sup>-1</sup> for the  $k=4$  ring to  $2 \times 10^8$  m s<sup>-1</sup> for the  $k=1$  ring. To form an ion beam, a carefully designed extraction system is installed on the source [Dougarg-Jabon *et al.* 1998]. This is presented in details elsewhere [Dougarg-Jabon *et al.* 2001]. In addition, creating better conditions for negative ion production, the discharge plasma can be enriched with electrons of low energy, due to two systems of heated tungsten filaments 0.3 mm in diameter [Velasco *et al.* 2015].

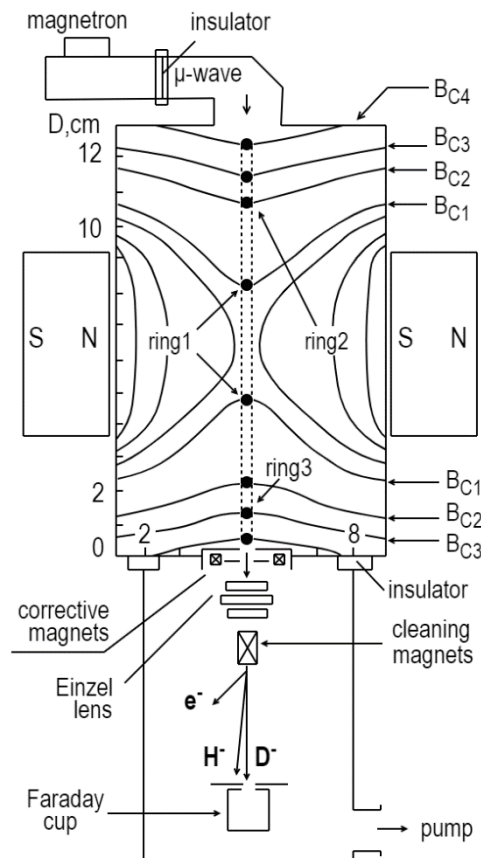


**Figure 12.19.** Assembly of the discharge chamber with the extraction system, concerning the ECR source with stratified plasma. Redrawn from [Dougár-Jabon 2001].

The source has been operated with hydrogen and deuterium. The main part of the discharge is occupied by plasma with a volume averaged density of around  $5 \times 10^{16} \text{ m}^{-3}$  and an electron temperature of 50-60 eV ( $2.66 \times 10^{-2} \text{ Pa}$  of  $\text{H}_2$ ; 200 W) [Dougár-Jabon *et al.* 1998]. **Fig. 12.20(a)** shows the dependence of the  $\text{H}^-$  and  $\text{D}^-$  currents at a microwave power of 200 W on the gas pressure, when the ring corresponding to the second harmonic of the fundamental electron cyclotron frequency touches the plasma electrode (upper electrode of the extraction system in **Fig. 12.19**). For both types of negative ions, a maximum is observed within the narrow pressure range of  $(2.66 \text{ to } 3.99) \times 10^{-4} \text{ Torr}$ . The  $\text{H}^-$  ion current is higher all over the pressure range. In this figure, the experimental conditions regarding the positive ion current are identical with those for the negative ions, with the exception of the extraction voltage polarity. Then, **Fig. 12.20(b)** unveils that the intensity of the  $\text{D}^-$  ion beam falls faster than the  $\text{H}^-$  one as the microwave power is diminished. This keeps true for the entire pressure range of **Fig. 12.20(a)**. Finally, **Fig. 12.20(c)** gives the  $\text{H}^-$  and  $\text{D}^-$  ion extracted current as a function of the plasma electrode immersion depth into the discharge chamber (up to 1.3 cm). These curves show clearly that the generation of both  $\text{H}^-$  and  $\text{D}^-$  ions with a high efficiency does not take place until one of the rotating rings enters into direct contact with the plasma electrode. The peaks for  $k = 3$  and  $k = 4$  illustrate cases when the plasma electrode comes into contact with the respective cyclotron harmonic rings.

These results testify that the vast majority of the negative ions are not formed through the capture of the plasma electrons, since they have too high energy to promote dissociative attachment directly, and that the plasma electrode surface plays a critical role, since its immersion into the plasma affects the negative ion extracted currents. Thus, it has been demonstrated [Dougár *et al.* 1998] that the negative ion generation mechanism is the volume vibrational excitation of hydrogen molecules, due to the energetic electrons, followed by the dissociative attachment of the electrons emitted by the plasma electrode under ion flux bombardment. In a more recent study [Dougár-Jabon 2001], the importance of the molecules excited to high-lying Rydberg states was considered to be higher than that of the vibrational excited ones, while the role of the secondary electrons was once more underlined.

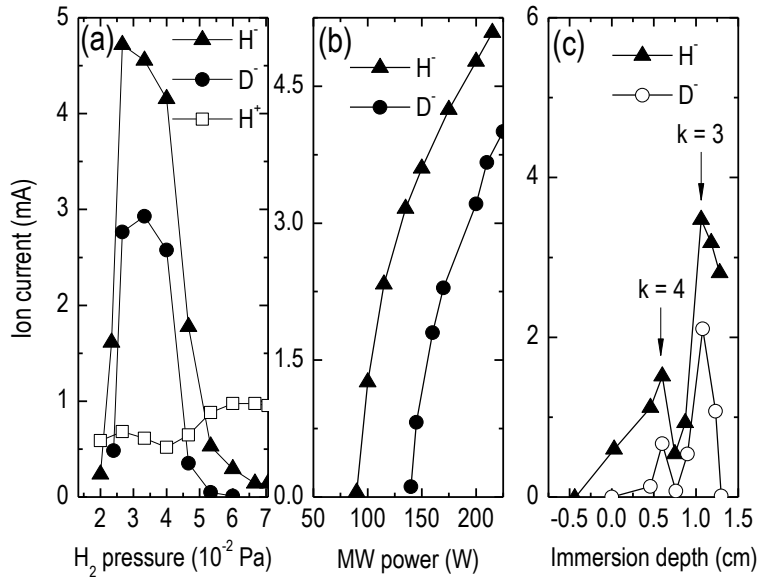


**Figure 12.20** Variation of the extracted negative ion currents as a function of (a) gas pressure (200 W), (b) microwave power ( $3.33 \times 10^{-2}$  Pa), and (c) the immersion depth of the plasma electrode ( $2.66 \times 10^{-2}$  Pa; 175 W). Redrawn from [Dougarg-Jabon 2001].

### 12.3.4 HOMER

A schematic representation of the ECR configuration called HOMER (HOMogeneous Electron cyclotron Resonance plasma) is given in Fig. 12.21, while details are given in [Rauner et al. 2015; Kurutz and Fantz 2015]. It consists of a cylindrical vacuum chamber having a height of 31 cm and a 7.5 cm radius, manufactured in stainless steel. The microwave (2.45 GHz) power, generated by a magnetron having a maximum power output of 1 kW, is transmitted through a borosilicate window from the top side of the vessel. An axial magnetic field of 87.5 mT, needed for electron cyclotron resonant heating, is generated homogeneously over the whole volume by two water-cooled solenoids located at the top and the bottom of the vacuum vessel.

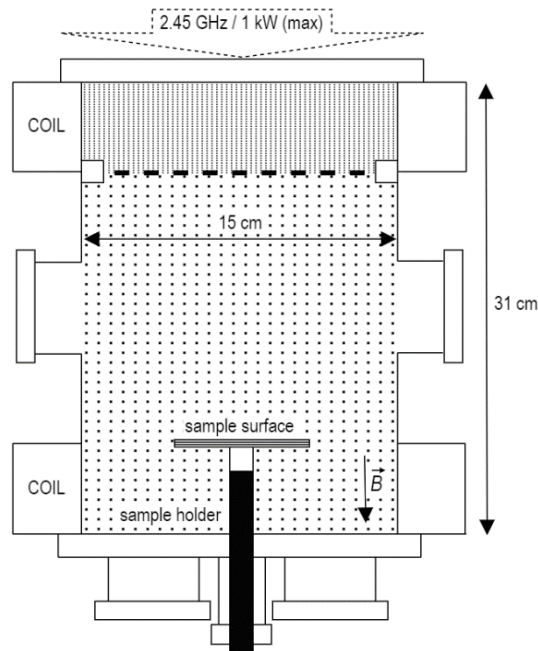


**Figure 12.21.** Concept of the basic version of the small scale, test bed HOMER. Redrawn from [Kurutz and Fantz 2015].

HOMER is equipped with a meshed grid located just below the first field coil. This mesh prevents the microwave from expanding into the lower part of the chamber, thereby applying the tandem principle, i.e. by dividing the source into two regions: the heated, driver region at the top (height 12 cm), and the non-heated, diffusive region extending over the lower part (height 19 cm). This method has the advantage that no additional magnetic fields are required which interfere with the already present magnetic field of the ECR setup [Kurutz *et al.* 2017]. Furthermore, the destruction of negative ions due to electron detachment in the downstream section below the grid is reduced. The grid potential can be biased relative to the grounded walls or set to be floating for influencing the diffusion of charged particles through the grid. Dedicative investigations regarding the influence of the meshed grid on the plasma parameters at HOMER are given by [Kurutz and Fantz 2015]. In the downstream region, the source is also equipped with the necessary viewports for the simultaneous installation of different diagnostics. In the diffusive downstream region beneath the meshed grid a horizontal oriented sample holder of 8.5×6 cm<sup>2</sup> made of stainless steel is located. The sample holder is thermally and electrically insulated and its axial position is variable. Samples can be heated up to 800 °C via heating elements inside the sample holder, while the sample holder bias can be modified relative to the grounded walls or the meshed grid affecting the energy of charged particles impinging on the investigated samples [Kurutz and Fantz 2015]. Later on [Friedl *et al.* 2020] introduced a prolonged vessel for light in sight optical emission spectroscopy measurements in both the heated and expanding parts of the plasma. Although more extensive studies have undergone for a hydrogen plasma, deuterium discharges have also been regularly studied in HOMER. The diagnostics used to determine the plasma parameters in each case include Langmuir probes, laser induced photodetachment, cavity ring-down spectroscopy, and optical emission spectroscopy. A detailed description of these setups and the application of each diagnostic technique may be found in the works cited in the current section.

The produced hydrogen and deuterium plasmas in HOMER, in the investigated pressure range of 0.3-3 Pa, are in general characterized by an electron density between 10<sup>16</sup>-10<sup>17</sup> m<sup>-3</sup>, an electron temperature (in the diffusive region) of about 1-2 eV, and a neutral atomic density,  $n_H$ , in the range 10<sup>18</sup>-10<sup>19</sup> m<sup>-3</sup> [Kurutz and Fantz 2015]. Furthermore, in the same pressure range and at varying microwave power between 200 W and 500 W, the maximum negative ion hydrogen density equals 3.9×10<sup>15</sup> m<sup>-3</sup> [Rauner *et al.* 2015].

Changing from H<sub>2</sub> to D<sub>2</sub>, both the ion density and the atomic density are increased in D<sub>2</sub>. The increased positive ion density is directly linked to a higher electron density and it can be explained by a better coupling of the microwave to the deuterium plasma. The increased atomic density is attributed to the higher dissociative cross section for D<sub>2</sub>. Other plasma parameters like gas temperature, the EEDF or the vibrational distribution of the molecular ground state show only very slight differences between the isotopes. Regarding negative ion formation, the higher electron density in D<sub>2</sub> indicates an enhanced negative ion volume production compared to H<sub>2</sub>. On the other hand, the higher atomic density in deuterium results in a comparably enhanced negative ion destruction within the volume due to the associative detachment process but also to an increased atomic flux onto the surface. Due to the only limited contribution of surface production in this case, the different effects seem to compensate each other leading to virtually identical negative ion densities in D<sub>2</sub> and H<sub>2</sub> [Friedl *et al.* 2017].

A large portion of the experimentation carried out at HOMER has been devoted to the investigation of the influence of various sample materials facing the plasma on negative ion production, either it be indirect by enhanced volume production, or direct by enhanced surface production [Friedl *et al.* 2017; Kurutz and Fantz 2015; Kurutz *et al.* 2017]. The main motivation behind these studies is the desire to find an alternative material to cesium (Cs) which can be efficient enough to be utilised in future negative ion sources. The main results are summarized in **Fig. 12.22**. Among the investigated Cs-free materials neither any of the investigated diamond materials nor bulk samples made of tantalum nor tungsten resulted in an enhanced negative ion density relative to the pure volume reference case. Moreover, all diamond materials significantly influenced the bulk plasma and showed clear signs of plasma-induced erosion. Hence, these materials cannot be seen as alternatives to the application of Cs [Kurutz *et al.* 2017]. In contrast, both low work function materials MoLa and LaB<sub>6</sub> lead to systematically increased negative ion density compared to the pure volume reference case [Kurutz *et al.* 2017]. Measured negative ion densities furthermore exceeded those expected from modelling of the volume processes, which indicates a direct negative ion surface production.

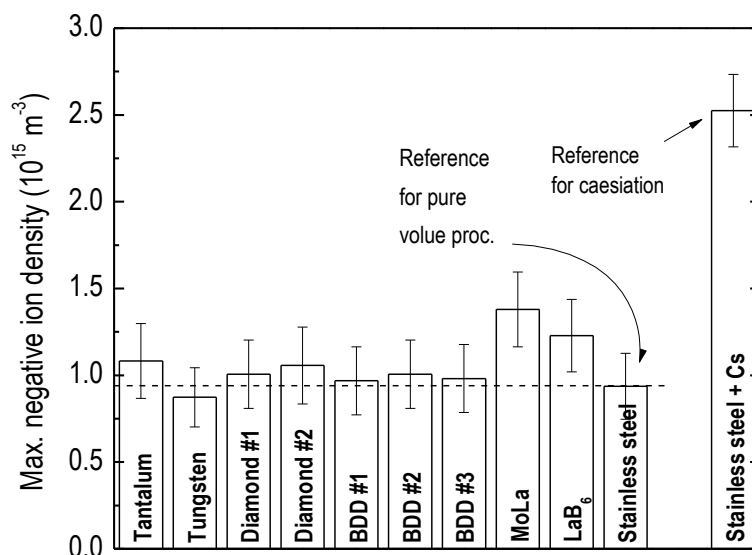


**Figure 12.22.** Maximal measured negative ion density for different materials at the same external experimental conditions: measured in a distance of 2.5 cm to unbiased samples, at 0.3 Pa  $\text{H}_2$  pressure and 300 W discharge power. Redrawn from [Kurutz *et al.* 2017].

In another report [Friedl *et al.* 2020], an extensive spectroscopic study of a hydrogen discharge (HOMER) coupled with collisional radiative modelling highlights the possibility of identifying individual contributions of the different excitation channels for the Balmer series. In low pressure, low temperature hydrogen plasmas electron impact excitation, dissociative excitation and dissociative recombination are prominent excitation channels for the Balmer series. These processes can have a specific influence on the translational energy of excited atoms which is correlated with the width of the respective line profiles. On this basis, an elaborate analysis of the Balmer emission lines' profiles from the diffusive region of the hydrogen plasma reveals that the dissociative recombination channel has a significant contribution to the excitation of the Balmer series and gives rise to a broad component in the line profiles of all the Balmer lines. Moreover, it is demonstrated and emphasized that the use of the simple line-ratio method ( $\text{H}_\gamma / \text{Fulcher}$ ) for the determination of the hydrogen atomic density can lose its validity if processes like the latter are neglected.

### 12.3.5 ROSAE (I, II, and III)

ROSAE (ecR HydrOgen plaSma for neutrAl bEam) reactors (versions I, II, and III) has been designed to study interaction processes between  $\text{H}_2$  and  $\text{D}_2$  plasmas and plasma-facing materials, with a special focus on the recombinative desorption mechanisms (see **Table 12.2**). In ROSAE I, seven elementary, dipolar, plasma sources, like those of **Fig. 12.6**, are installed above a Pyrex™ cylinder (200 mm in diameter and 200 mm in height). The Pyrex™ cylinder is housed in the Camembert III vacuum chamber **Fig. 12.23(a)** [Bacal *et al.* 2004]. The plasma is produced in the electronic cyclotronic resonance (2.45 GHz) regions of the elementary sources and diffuses in the Pyrex™ cylinder, preventing however its diffusion towards the vacuum chamber walls. A Pyrex™ disk is also placed at the bottom of the cylinder, leaving thus as plasma entrance only the upper, open side of the cylinder. This arrangement is presented in **Figs. 12.23(b)** and **(c)**. The aim of the Pyrex™ cylinder is the creation of a smaller volume of plasma than the one produced in the Camembert III chamber, in order to promote surface reactions with samples of limited size (48 mm in diameter); see sample holder in **Fig. 12.23(d)**. In the Camembert III chamber the surface to volume ratio is close to 0.005, while in ROSAE I it equals 0.025. As it is seen in the photos of **Figs. 12.23(b)** and **(d)**, the sample forms a detachable part of the Pyrex™ cylinder wall, while a load lock chamber is used for the sample interchange under vacuum conditions. In addition, the sample temperature is controllable by means of a closed loop system and the sample electrical potential may be biased.

The reference material is a disk of Pyrex™. Three different materials have been investigated: Pyrex™, graphite (HOPG), and tantalum (Ta), at the same total microwave power (1 kW) and at hydrogen pressure 0.8 Pa. Conventional electrostatic probes and laser induced photodetachment are employed for the plasma interrogation.

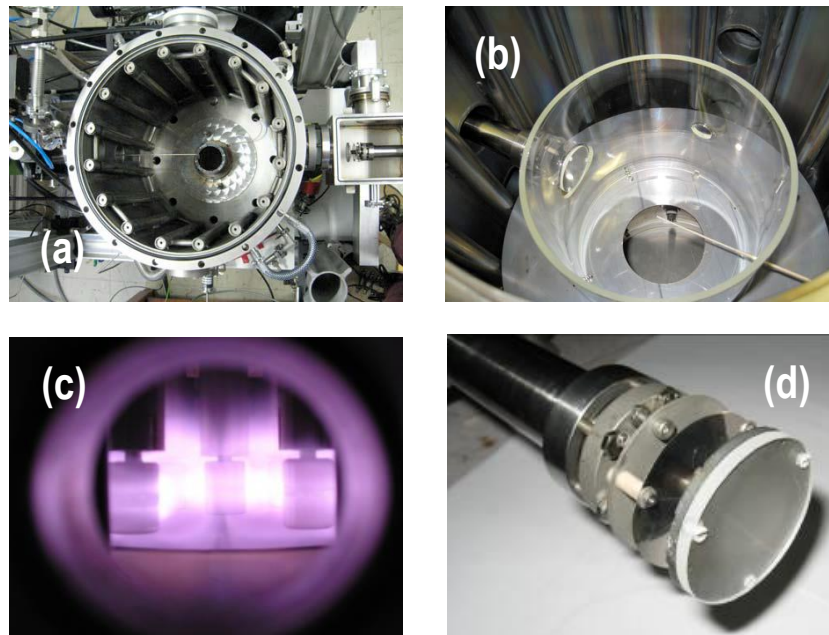


**Figure 12.23.** (a) The interior of the Cabembert III multi cusp chamber. (b) The Pyrex™ cylinder installed at the center of the Camembert III chamber. (c) Photo of three (out of seven) elementary plasma sources in operation. (d) Sample holder, where a Pyrex™ specimen (48 mm in diameter) is mounted.

Despite the small surface ( $0.007 \text{ m}^2$ ) of the samples, compared to the whole Pyrex™ cylinder surface facing the plasma ( $0.16 \text{ m}^2$ ), measurements of the peak of the photodetached electron signals versus the sample temperature show observable differences (each signal peak is reduced to the background electron density current and this ratio provides an analogy to the negative ion density [Bacal 2000]). A significant increase of 26% has been obtained for the HOPG samples between 263 and 293 K. For the Ta samples, a less significant variation has been mentioned within the same temperature range. The Pyrex™ samples have induced the largest increase, i.e. 45%, when the temperature increases from 263 to 393 K. These results can be interpreted as the variation of the recombination coefficient of H atoms ( $\gamma_H$ ), which varies with the temperature differently in the case of on the Pyrex™ or metals. For Pyrex™ and Quartz, previous results [Wood and Wise 1958; Wood and Wise 1961] indicate an important variation of the  $\gamma_H$  coefficient as a function of the surface temperature. As a matter of fact, it decreases from about  $10^{-3}$  down to  $2 \times 10^{-5}$  for a temperature increase between about 75 and 115 K, whereas it rises monotonously up to  $3 \times 10^{-2}$  when the temperature approaches 500 K. On the contrary, in the case of metals, recombination coefficient  $\gamma_H$  is not affected by the temperature variation between 300 and 1000 K [Taccogna *et al.* 2007] and stays close to 0.5.

In response to the preliminary, encouraging results obtained in ROSAE I, a second prototype was developed (ROSAE II), which led finally to the experimental setup ROSAE III (Fig. 12.24). The ROSAE III structure consists of a stainless steel cylindrical chamber of 150 mm in diameter. It houses a Pyrex™ cylindrical shell being 140 mm in diameter and 200 mm in height, defining thus a surface to volume ratio equal to 0.038. Either one or four dipolar sources, like those of Fig. 12.6, can be adapted to the upper flange of the chamber. These sources pass through a Pyrex™ disc facing the plasma, i.e., covering the inner surface of the top stainless steel flange. As Fig. 12.24 depicts, the specimens are in the form of sheets (0.1 mm in thickness), made of bulk material. Stainless steel (SS), tantalum (Ta), and tungsten (W) have been tested. Plasma has been probed by means of electrostatic probes, laser induced photodetachment, and optical emission spectroscopy. Representative results are given in Fig. 12.25.

Comparative measurements before and after mounting the SS sheet opposite to the plasma source, do not show any particular effect on the plasma density  $n_e$  in position B (Fig. 12.24) where negative ions are formed by DA of cold electrons. Additionally, at the same position, the electron energy  $kT_e$  ranges from 0.9 to 1.3 eV [Bentounes *et al.* 2018] when the delivered microwave power increases between 75 and 175 W. This holds true independently of the plasma facing material (Pyrex™ or SS). Although  $n_e$  and  $kT_e$  are not affected by the plasma facing material, the  $\text{H}^-$  negative ion density

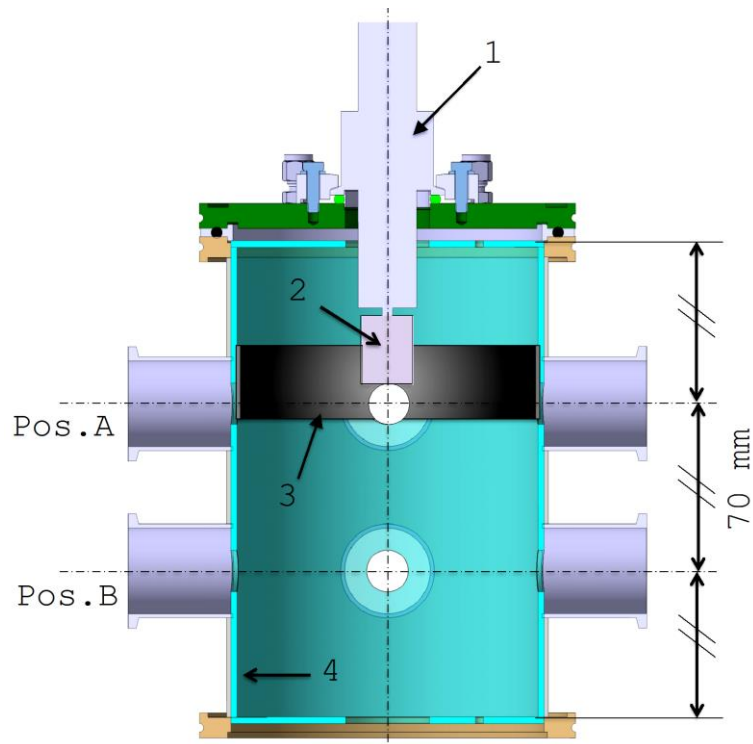


**Figure 12.24.** ROSAE III conceptual design (vertical section). (1): dipolar plasma source; (2): permanent magnet; (3): mounted specimen in the form of sheet; (4): Pyrex™ shell.

$n_{H^-}$  highly does. **Fig. 12.25(b)** presents the variation of this quantity versus the microwave power at two different pressures, i.e., 0.8 and 1.6 Pa. In the Pyrex™ case,  $n_{H^-}$  is not significantly affected neither by the microwave power nor by the hydrogen pressure, remaining close to a value of about  $5 \times 10^{13} \text{ m}^{-3}$ . Though, the stainless steel specimen leads to an almost fivefold value of  $n_{H^-}$ , i.e., negative ion density up to about  $2.5 \times 10^{14} \text{ cm}^{-3}$  is achieved at 1.6 Pa.

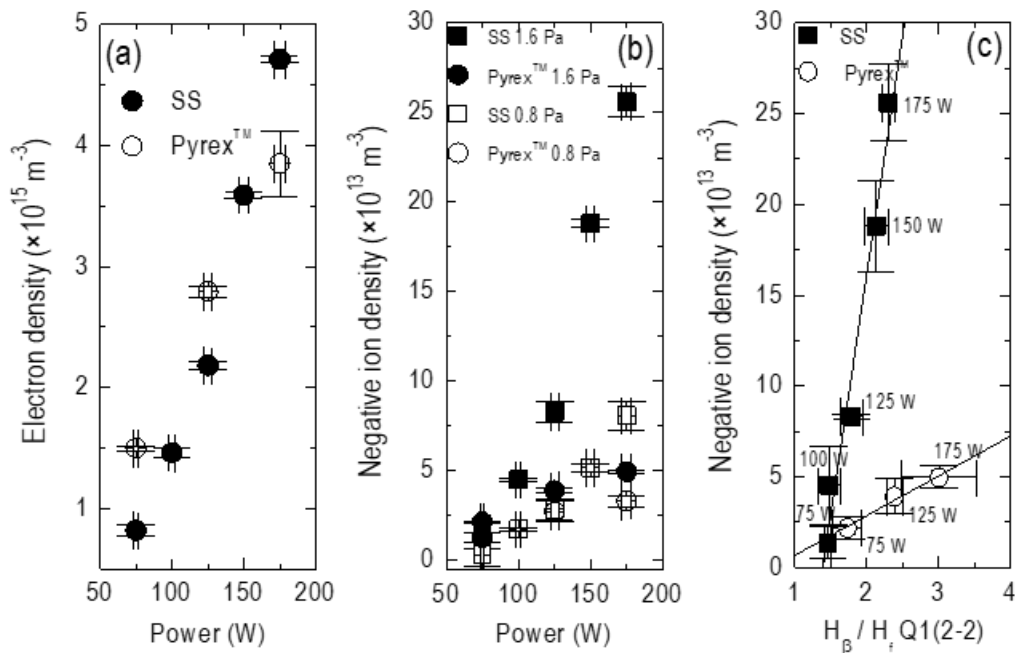


**Figure 12.25.** Basic plasma parameters in ROSAE III, in the cases of Pyrex™ and stainless steel (Pos. B – Fig. 12.24; single dipolar plasma source). **(a)** Electron density vs. power (1.6 Pa). **(b)** Negative ion density vs. power, at 0.8 and 1.6 Pa. **(c)** Negative ion density vs. the  $H_\beta$  to  $H_{\text{fulcher}} Q_1(2-2)$  intensity ratio, at different power levels (1.6 Pa).

The observed increase in the negative ion density in the case of the stainless steel sheet, may be considered with respect to the data given in **Fig. 12.25(c)**. It is proposed that either the SS sheet increases the ro-vibrational molecular density (at the same plasma density and electron energy) or that it decreases the atomic density. Following the first assumption, the sheet increases the production of negative ions through DA, whereas, following the second assumption, it decreases the destruction of negative ions due to collisions with H atoms. The  $H_{\beta}$  to  $H_{\text{fulcher}Q_1(2-2)}$  intensity ratio, i.e., the ratio of the intensity of the radiative transitions Balmer( $n = 4 \rightarrow 2$ ) and  $d^3\Pi_u \rightarrow \alpha^3\Sigma_g^+$  respectively, may provides the relative density of H atoms [Fantz *et al.* 2006]. In **Fig. 12.25(c)**, for a mutual atom to molecule ratio, e.g. 2.5, the negative ion density is lower than  $5 \times 10^{13} \text{ cm}^{-3}$  with Pyrex™, whereas it becomes higher than  $2.5 \times 10^{14} \text{ cm}^{-3}$  with the SS sheet. This demonstrates the efficient increase of negative ion via DA. In order to investigate the production of ro-vibrational excited molecules, the following (SCHEME) reactors were designed.

### 12.3.6 SCHEME (I, II, and III)

The SCHEME (Source of exCited HydrogEn MolEcules) reactors (versions I and II) have been designed for dedicated studies on plasma-surface interactions, using synchrotron radiation. The ratio of the plasma-facing surface to the plasma volume equals 0.04, which is practically the same as in ROSAE III reactor (i.e., 0.038). However, to improve the temperature control of the plasma-facing surfaces, a copper cooling cylinder interfaces both a stainless steel chamber and a glass cylindrical shell, with the latter to be made of Quartz (aluminosilicate glass, Schott™ 8250, 3 mm thick).

The concept design of the SCHEME I reactor is shown in **Fig. 12.26**. The above mentioned, Quartz cylinder is 124 mm in diameter and 150 mm in height, while it is ended by a Quartz disk on both sides. This amorphous glass surface serves as a reference surface of low atom recombination coefficient ( $\gamma_H = 0.004$  at 290 K). Hence, ro-vibrationally excited molecules are created essentially in the ECR coupling zone close to the permanent magnet of the dipolar plasma source (see details “c” and “d” in **Fig. 12.26**). In order to study other materials, tantalum (Ta), tungsten (W) and stainless steel (SS) foil of the material under consideration (0.1 mm thick) is flattened on the inner surface of this Quartz tube. The temperature of the Quartz and the specimen temperature are controllable and maintained at 288 K. This keeps the atom recombination coefficient of the Quartz cylinder as close as possible to 0.004 and thus prevents recombinative desorption on its surface. At the same time, over the temperature range between 240 and 300 K, metallic surfaces have a higher recombination coefficient ( $\gamma_H \approx 0.5$ ) and thus promote surface recombination of atoms originating in the plasma volume. As the investigated material (Ta, W or SS) is placed on the Quartz surface, its potential is floating, which does not induce a potential modification between Quartz and metallic surfaces.

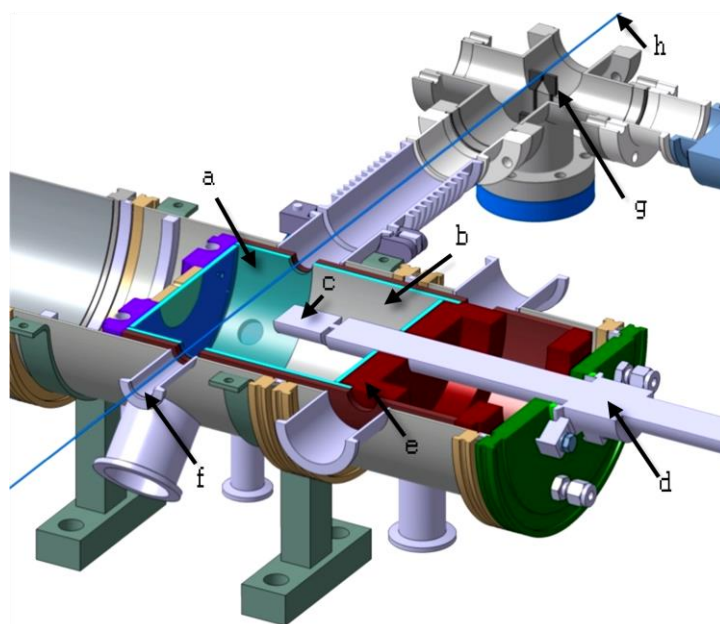


**Figure 12.26.** SCHEME I conceptual design (horizontal section). (a): Quartz cylinder; (b): mounted specimen; (c): permanent magnet; (d): dipolar plasma source; (e): cooling copper; (f): solar blind photoelectron multiplier tube position; (g): tuning fork – optical chopper; (h): radiation beam.

For the last eight years, the SCHEME I setup was transported and temporarily installed at the SOLEIL synchrotron (France), as part of experimental campaigns with the objective of using VUV radiation to study the molecular hydrogen excitations in plasmas. SCHEME I setup was installed on the branch B end station (delivering a monochromatized beam) of the DESIRS (Dichroïsme Et Spectroscopie par Interaction avec le Rayonnement Synchrotron) beam line of the synchrotron for conducting absorption spectroscopy experiments. DESIRS is an undulator based beamline covering the VUV range (5 - 40 eV) with a unique combination of ultra high resolution spectral purity, flux and fully variable polarization [de Oliveira *et al.* 2009; de Oliveira *et al.* 2011]. During these first experiments, a solar blind photoelectron multiplier tube, with MgF<sub>2</sub> window, was set on the radiation beam axis. The radiation beam was chopped by a tuning fork (oscillating at 130 Hz) for phase sensitive signal detection. This phase sensitive, lock-in detection, rejected the continuous stray light emitted by the plasma. These preliminary experiments [Béchu *et al.* 2017] were carried out by using three hot tungsten filaments in the glass chamber, instead of a plasma source. H<sub>2</sub> molecules were partially dissociated into atoms following thermal and catalytic effects sustained by the hot filaments. Hence, even if dissociation was less effective, light coming from the filament **was essentially in the infrared range and less excited species had to be considered**. In order to isolate the synchrotron beam line (very low pressure) from glass chamber (H<sub>2</sub> pressure), a MgF<sub>2</sub> windows was inserted in the position “h” (Fig 12.26). Following this initial campaign, information obtained by laser induced fluorescence and synchrotron radiation absorption, gave the first stepping stones for further experimental adjustments to increase spectral resolution. Such an improvement was obtained when the 2400 grooves mm<sup>-1</sup> grating of the 6.56 m normal incidence monochromator of the branch B was employed. Thus, with both entrance and exit slits set at 50 μm, a resolution of 30 mÅ was achieved.

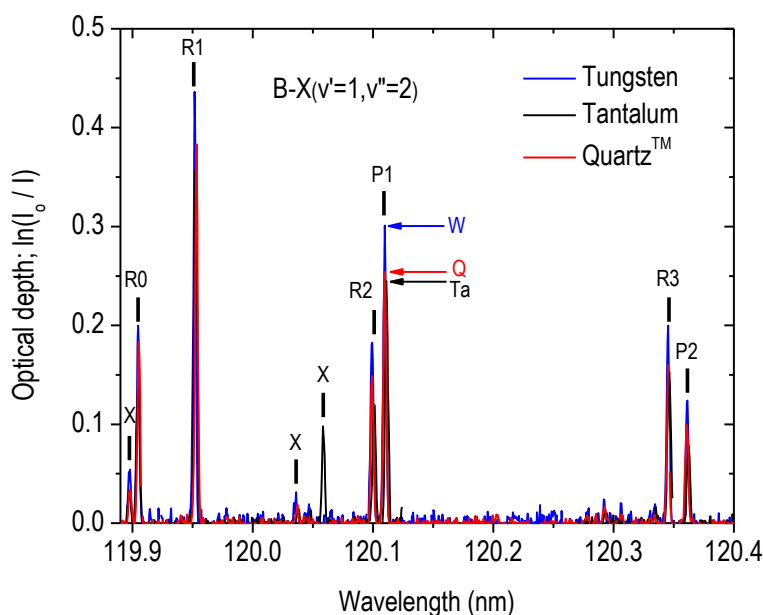


**Figure 12.27.** Synchrotron beam absorption spectra (optical depth) of hydrogen ECR plasma faced by three different materials: Quartz (red); Tungsten (blue); Tantalum (black). 1.6 Pa; 150 W.

**Figure 12.27** summarizes the main results obtained with this high resolution setting on the branch B. It shows a few rotational transitions of the vibrational BX( $v' = 1 \leftarrow v'' = 2$ ) transition, proving thus that the  $v'' = 2$  vibrational level of the electronic ground state (at about 10.419 eV) is populated. Rovibrational transitions have been recorded in the ECR plasma for three different specimens (detail “b” in Fig. 12.26): quartz, tungsten and tantalum. Significant differences are observed, and particularly in the tungsten case. In addition to the transition BX( $v' = 1 \leftarrow v'' = 2$ ), which characterizes the population  $v'' = 2$  level of the electronic ground state, similar spectra have been recorded for the three materials up to the transitions BX( $v' = 1 \leftarrow v'' = 3, 4, 5, 6$ ). All these transitions were selected on the basis of favourable Franck-Condon factors [Fantz and Wunderlich 2006].

It was clearly understood with these first experiments that increased spectral resolution was needed (from 3.0 to 0.7 pm, FWHM), in order to separate most of the H<sub>2</sub> observable lines, and also to reduce the long acquisition time required by the wavelength scanning of the monochromator. It was thus required the use of the high resolution VUV Fourier transform spectrometer (FTS) permanently installed on the same DESIRS beam line [Béchu *et al.* 2020]. An other advantage lied in the relatively fast recording time to get a complete spectrum. A second advantage was the access to the full VUV range without any window, at the expense nevertheless of two additional differential pumping set. They were placed, in combination with thin diaphragms (0.1 mm thick and 3 × 5 mm aperture), as close as possible to both sides of the reactor in addition to the pumping sets already provided for safety on the SR beam exit and of the FTS entrance. With 50 l s<sup>-1</sup> turbo pumps it was possible to work up to 0.8 Pa with H<sub>2</sub>. For that purpose, an updated reactor (SCHEME II; Fig. 12.28) was developed, based on the initial concept of SCHEME I.

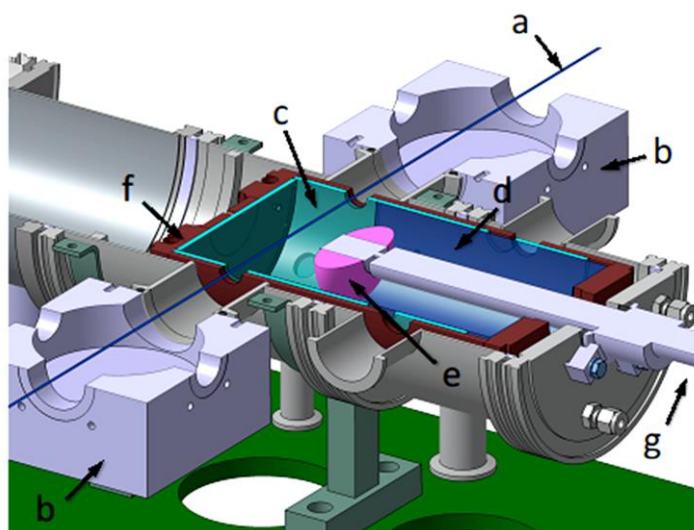


**Figure 12.28.** SCHEME II+ conceptual design (horizontal section). (a): radiation beam; (b): differential pumping system; (c): Quartz shell; (d): mounted specimen; (e): ECR coupling zone; (f): cooling copper; (g): dipolar plasma source.

Thanks to these modifications, spectra measurements down to wavelengths as short as 90 nm were used to scan both the H Lyman alpha lines and the BX( $v' = 0$ ) molecular lines up to high  $v'$ . Hence, dissociation ratio of the molecular gas was measured as well as the densities of rotational states of the gas ( $v'' = 0$ ) in plasma OFF and ON conditions. These measurements, corresponding to a calibration procedure, were mandatory to get absolute distribution of ro-vibrational states ( $v' = 0, v''$ ) in the plasma. An even higher pumping capacity (upgraded to 300 l s<sup>-1</sup>) was achieved with slight modifications in the original design of SCHEME II (hence named SCHEME II+ in Fig. 12.28). The improved setup, in a subsequent run, allowed measurements in windowless mode up to 3.2 Pa while keeping the pressure as low as below 10<sup>-5</sup> Pa outside the reactor.

In order to cover the BX( $v' = 0, v'' = 0 - 8$ ) transitions in the 65000 to 97500 cm<sup>-1</sup> energy range (Fig. 2.29), as the energy coverage of an undulator setting was close to 3500 cm<sup>-1</sup> (FWHM), nine overlapping settings were used for scanning the ro-vibrational components at the quantum levels  $v''$  with a spectral resolution of 0.95 pm. The sampling rate was 512 kSamples, allowing a recording of this spectral range within about 120 min. Different materials (Quartz as a reference surface; Ta; W; and SS) were studied at three pressures (0.8, 1.6 and 3.2 Pa), two power levels (150 and 250 W), and two gases (H<sub>2</sub> and D<sub>2</sub>). Before each series of measurements with a specific material, a cleaning of the investigated surface with plasma (gas mixture of Ar and H<sub>2</sub> or D<sub>2</sub>), sustained for 10 min, was performed, followed by 15 min of warming up in pure H<sub>2</sub> or D<sub>2</sub>. As the plasma source was movable along its axis, different positions inside the reactor could be used to probe the plasma in the plasma source vicinity while the synchrotron beam location was constant. The most significant results are given below, whereas complete results could be found in already published papers [Bentounes *et al.* 2018; Béchu *et al.* 2017; Béchu *et al.* 2020] or they will be published soon.

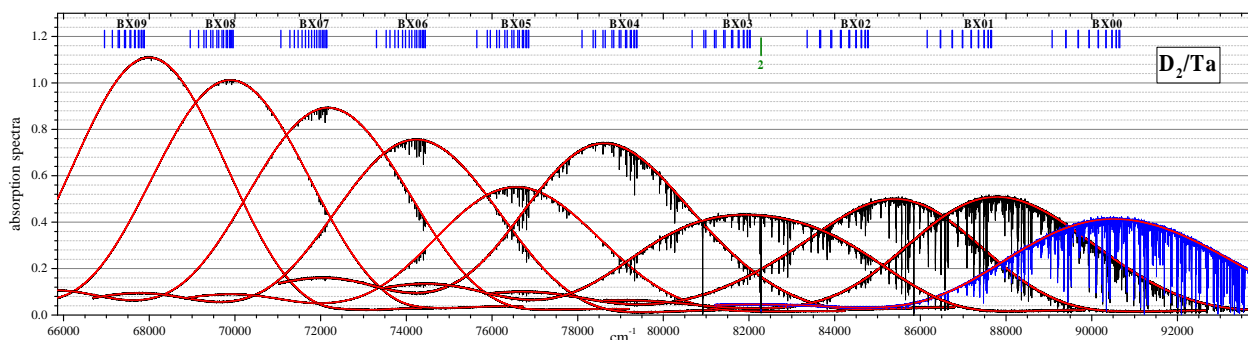


**Figure 12.29.** Absorption spectra (black), fitted continua (red) in the different Gaussian-like spectral windows (corresponding to different undulator settings) used to record the  $D_2^*(v' = 0, v'' = 0 - 8)$  transitions of the  $D_2^*(v'', J'')$  molecule (data obtained with SCHEME II+ reactor).

Under these improved experimental conditions, all Lyman transitions below Lyman- $\alpha$  (also called Ly-1) that are not partially or fully blended by molecular lines became observable. **Fig. 12.30** presents absorption lines of Ly-3 up to Ly-8, i.e., from 97.2517 down to 92.3148 nm. The oscillator strengths of these lines are much more lower than Ly-1 which avoids line saturation. Indicatively, at 0.8 Pa and 150 W, the absolute density of H atoms was found to be  $3 \times 10^{19} \text{ m}^{-3}$  with full Quartz versus  $1.3 \times 10^{18} \text{ m}^{-3}$  with a Ta specimen.

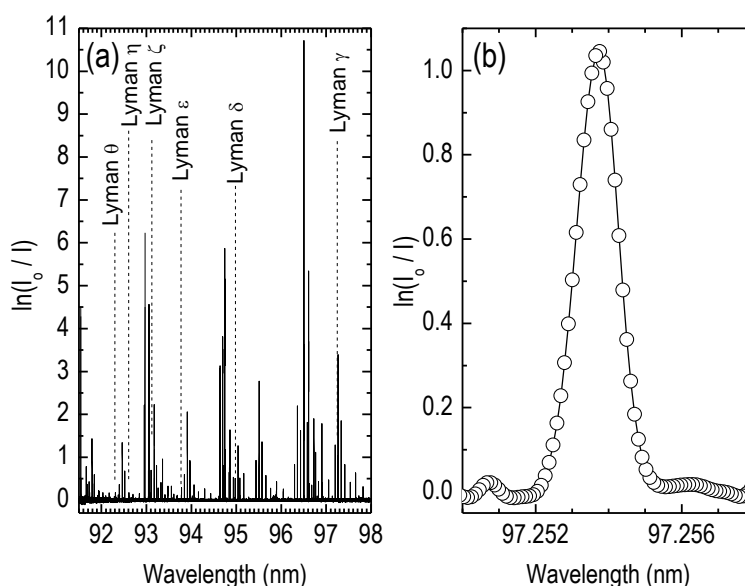


**Figure 12.30.** (a) Optical depth of  $H(n=1)$  obtained at 150 W and 0.8 Pa, using Quartz in the SCHEME II+ reactor. (b) Focus on the Lyman- $\gamma$  transition.

**Fig. 12.31** shows, after data processing, the VUV excited deuterium optical depth,  $\ln(I_0 / I)$ , with respect to the wavenumber, obtained in the spectral window centered at  $74200 \text{ cm}^{-1}$ . In addition to the BX06 band, the BX27 band is observed in its wing. In fact, all band data obtained inside the FWHM of a given undulator setting were useful with a good signal-to-noise ratio depending also on the oscillator strength of the transition.

Hence, by carefully observing the spectra, additional vibrational transitions can be unveiled, i.e.  $BX(v' = 1 - m, v'' = 0 - n)$ , on the top of  $BX(v' = 0, v'' = 0 - n)$ . They were used to improve the accuracy of the results, allowing a better identification of the role of the different materials in populating the vibrational distribution functions (VDFs) of hydrogen (or deuterium) in the plasma. Among the 121  $BX(v' = 0 - 10, v'' = 0 - 10)$  potentially observable transitions, about 58 were useful to accurately determine, in conjunction with the FC factors, the vibrational populations in each  $v''$  level of the ground state, then giving access to the VDF of the plasma. The calibration was made by using the  $BXv'0$  data obtained without plasma (see details in [Béchu et al. 2020]).

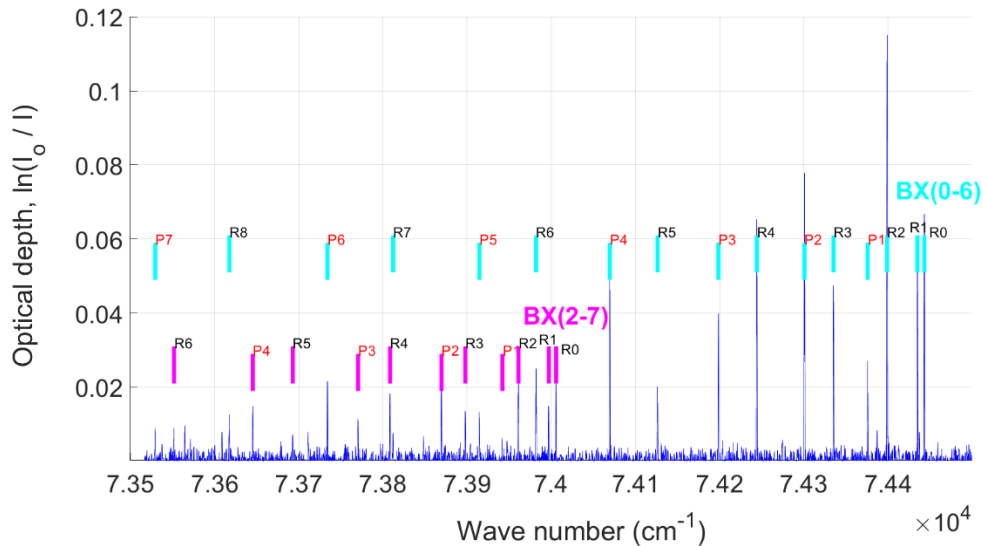


**Figure 12.31.** Optical depth of the  $D_2(v' = 0, v'' = 0 - 6)$  transition of the  $D_2^*(v'', J'')$  molecule in the plasma (data obtained with Ta, at 150 W and 0.8 Pa, in the reactor SCHEME II+).

Thus, the spectra were processed in such a way to obtain an absolute vibrational distribution function which allowed for an overall comparison for the different vibrational quantum levels, when different materials were tested. An example is given in **Fig. 12.32**, showing that Ta promotes a higher production of quantum levels above  $v'' = 3$ . An increase by 2.6 is seen for  $v'' = 7$ , as compared to Quartz. This experimental result shows similar trend with that reported by quantum dynamic calculations for graphite [Jackson and Lemoine 2001], where the average quantum number for molecules produced by recombinative desorption was found to be close to 8. On the other hand, for lower vibrational levels, Quartz yielded higher populations (e.g., by a factor of 1.7 at  $v'' = 0$ ). Complementary studies (laser photodetachment and electrostatic probe measurements) at similar conditions, have provided an analogous increase of negative ions whilst electron density remained nearly constant. In light of the results provided by this particular diagnostic technique (absorption of synchrotron radiation), the interpretation of previously published results [Bacal *et al.* 2004] can be further enhanced.

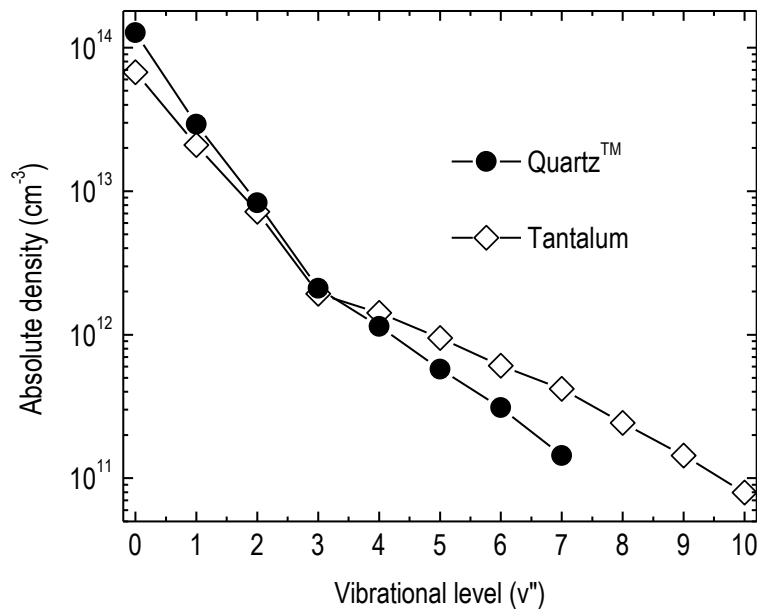


**Fig. 12.32.** Absolute vibrational distribution function in ECR  $D_2$  plasma, in the case of two different materials-specimens (0.8 Pa; 150 W). Reactor SCHEME II+.

#### 12.4. Other sources and Extracted currents in ECR sources

In this last paragraph of the present Chapter, additional ECR sources are touched upon and  $H^-$  negative ion extracted currents from different sources are compared.

At Argonne National Laboratory [Spence and Lykke 1998], the  $H^-$  and  $D^-$  ion source refers to a magnetically confined microwave driven (ECR) source, purchased from Atomic Energy of Canada, Ltd., which is powered by a 2.45 GHz microwave generator (2 kW). The microwave generator is coupled to the source via a circulator and a four-stub autotuner. The ion source is attached to a large, high vacuum, oil free diagnostic chamber with a base pressure of about  $1.33 \times 10^{-6}$  Pa. The mechanism for  $H^-$  ion production is via DA, while the initial production of  $H_2(v)$ , i.e., the precursor of  $H^-$ , is assumed to be by excitation of ground state molecules. However, in order to take advantage of the recombination desorption of hydrogen atoms on tantalum surface and, thus, enhanced  $H_2(v)$  population, a thin layer of Ta is sputtered on the inner surface of the source. Results confirm the importance of the recombination desorption mechanism to  $H_2(v)$  production. Finally, the total  $H^-$  ( $D^-$ ) ion current being extracted from the 5 mm diameter source aperture was estimated to be 4-5 mA (at 700 W cw), indicating little or no isotope effect.

At Peking University [Zhang *et al.* 2018], an improved with respect to a previous version, 2.45 GHz microwave driven (ECR) source, has been installed. The microwave is fed into the source chamber through a dielectric window made of three pieces of  $Al_2O_3$  and one piece of boron nitride to prevent electron bombardment. The ECR magnetic field is generated by a set of ring shaped Nd-Fe-B permanent magnets, surrounding the source chamber. Furthermore, a pair of filter magnets form a transversal filter magnetic field, separating thus physically the source into the ECR driving zone and the  $H^-$  ion formation zone. This Cs-free source yielded a maximum 8.5 mA pure  $H^-$  beam. The beam was extracted at 50 kV with the time structure of 100 Hz / 0.3 ms. The emittance (rms) of the beam was  $0.25 \pi$  mm mrad. The improved  $H^-$  ion source and extraction system were maintenance free for more than 200 h in operation. Once again, negative ions was assumed to be produced via DA, while a tantalum lining with thickness of 0.1 mm was installed inside the whole source chamber to enhance the  $H_2(v)$  production.

At Saclay [Gobin *et al.* 2006], two coils have been used to provide an axial magnetic field of 875G for the 2.45 GHz driven source. The magnetic coils are located around the source chamber. A protected Quartz window separates the standard WR284 rectangular waveguide, towards the plasma side, from the 1.2 kW magnetron microwave generator. A potential biased metallic grid has replaced the initial magnetic filter and allows for the separation of the  $H^-$  ion production zone from the ECR zone. The grid is connected to the plasma electrode and both are negatively biased with respect to the plasma chamber which is connected to negative high potential. The source has been designed to produce low energy beam in pulsed mode. The source typically operates at 1 to 2 ms at a frequency between 5 and 10 Hz. At typical working pressure (i.e., about  $2.66 \times 10^{-6}$  Pa in the extraction chamber, which corresponds to about 0.26 Pa in the plasma chamber) about 2 mA of  $H^-$  ion current has be extracted at 6 kV. These ions were collected on the Faraday cup through an aperture of 50 mm in diameter. The source reliability has been checked in pulsed mode (2 ms pulse width at a period of 100 ms) during 5 days and a continuous operation without any human intervention has been achieved. At much lower pressure in the extractor (i.e.,  $6.66 \times 10^{-4}$  Pa), 2.8 mA of  $H^-$  ion current has been claimed (see [Gobin *et al.* 2006] for discussion).

Finally, the source with driven plasma rings (Section 12.3.3) has yielded negative ion extracted current around 5 mA (Fig. 12.20) and the source Camembert III (Section 12.3.1) around 0.25 mA (Fig. 12.12).

## References

- Aleiferis S, Tarvainen O, Svarnas P, Bacala M, Béchu S, “Experimental investigation of the relation between H<sup>-</sup> negative ion density and Lyman- $\alpha$  emission intensity in a microwave discharge”, *J. Phys. D: Appl. Phys.* **49**, 095203 (2016)
- Aleiferis S, Svarnas P, Béchu S, Tarvainen O, Bacal M, “Production of hydrogen negative ions in an ECR volume source: balance between vibrational excitation and ionization”, *Plasma Sources Sci. Technol.* **27**, 075015 (2018)
- Asmussen J, Mak P, “Control of multipolar electron cyclotron resonance discharges using internal cavity impedance matching”, *Rev. Sci. Instrum.* **67**, 1753 (1994)
- Bacal M, Hillion F, Nachman M, “Extraction of volume-produced H<sup>-</sup> ions”, *Rev. Sci. Instrum.* **56**, 649 (1985)
- Bacal, M., “Photodetachment diagnostic techniques for measuring negative ion densities and temperatures in plasmas”, *Rev. Sci. Instrum.* **71**, 3981 (2000)
- Bacal M, Ivanov Jr A A, Glass-Maujean M, Matsumoto Y, Nishiura M, Sasao M, Wada M, “Contribution of wall material to the vibrational excitation and negative ion formation in hydrogen negative ion sources”, *Rev. Sci. Instrum.* **75**, 1699 (2004)
- Bacal M, “Physics aspects of negative ion sources”, *Nucl. Fusion* **46**, S250 (2006)
- Bacal M, Wada M, “Negative hydrogen ion production mechanisms”, *Appl. Phys. Rev.* **2**, 021305 (2015)
- Bacal M, Wada M, “Negative ion source operation with deuterium”, *Plasma Sources Sci. Technol.* **29**, 033001 (2020)
- Bacal M, Sasao M, Wada M, “Negative ion sources”, *J. Appl. Phys.* **129**, 221109 (2021)
- Bardsley J N, Wadehra J M, “Dissociative attachment and vibrational excitation in low-energy collisions of electrons with H<sub>2</sub> and D<sub>2</sub>”, *Phys. Rev. A* **20**, 1398 (1979)
- Baxter R J, Hu P, “Insight into why the Langmuir-Hinshelwood mechanism is generally preferred”, *J. Chem. Phys.* **116**, 4379 (2002)
- Béchu S, Soum-Glaude A, Bes A, Lacoste A, Svarnas P, Aleiferis S, Jr Ivanov A A, Bacal M, “Multi-dipolar microwave plasmas and their application to negative ion production”, *Phys. Plasmas* **20**, 101601 (2013)
- Béchu S, Aleiferis S, Bentounes J, Gavilan L, Shakhatov V A, Bès A, Svarnas P, Mazouffre S, de Oliveira N, Engeln R, Lemaire J L, “Detection of rovibrationally excited molecular hydrogen in the electronic ground state via synchrotron radiation”, *Appl. Phys. Lett.* **111**, 074103 (2017)
- Béchu S, Lemaire J L, Gavilan L, Aleiferis S, Shakhatov V, Lebedev Y A, Fombaron D, Bonny L, Menu J, Bès A, Svarnas P, de Oliveira N, “Direct measurements of electronic ground state ro-vibrationally excited D<sub>2</sub> molecules produced on ECR plasma-facing materials by means of VUV-FT absorption spectroscopy”, *J. Quant. Spectrosc. Radiat. Transf.* **257**, 107325 (2020)
- Bentounes J, Béchu S, Biggins F, Michau A, Gavilan L, Menu J, Bonny L, Fombaron D, Bès A, Lebedev Yu A, Shakhatov V A, Svarnas P, Hassaine T, Lemaire J L, Lacoste A, “Effects of the plasma-facing materials on the negative ion H<sup>-</sup> density in an ECR (2.45 GHz) plasma”, *Plasma Sources Sci. Technol.* **27**, 055015 (2018)

- Cacciatore M, Rutigliano M, "The semiclassical and quantum-classical approaches to elementary surface processes: dissociative chemisorption and atom recombination on surfaces" *Phys. Scr.* **78**, 058115 (2008)
- Cacciatore M, Rutigliano M, "Dynamics of plasma–surface processes: E–R and L–H atom recombination reactions", *Plasma Sources Sci. Technol.* **18**, 023002 (2009)
- Capitelli M, Cacciatore M, Celiberto R, De Pascale O, Diomede P, Esposito F, Gicquel A, Gorse C, Hassouni K, Laricchiuta A, Longo S, Pagano D, Rutigliano M, "Vibrational kinetics, electron dynamics and elementary processes in H<sub>2</sub> and D<sub>2</sub> plasmas for negative ion production: modelling aspects", *Nucl. Fusion* **46**, S260 (2006)
- Capitelli M, Celiberto R, Colonna G, Esposito F, Gorse C, Hassouni K, Laricchiuta A, Longo S, "Formation of Vibrationally and Rotationally Excited Molecules During Atom Recombination at Surfaces", *Fundamental Aspects of Plasma Chemical Physics*, Springer New York (2016)
- Celiberto R, Janev R K, Laricchiuta A, M. Capitelli, J. M. Wadehra, D. E. Atems, "Cross section data for electron–impact inelastic processes of vibrationally excited molecules of hydrogen and its isotopes", *At. Data Nucl. Data Tables* **77**, 161 (2001)
- Courteille C, Bruneteau A M, Bacal M, "Investigation of a large volume negative hydrogen ion source", *Rev. Sci. Instrum.* **66**, 2533 (1995)
- Dem'yanov A V, Dyatko N A, Kochetkov I V, Napartovich A P, Pal' A F, Pichugin V V, Starostin A N, "Properties of a beam-driven discharge in an H<sub>2</sub>-Ar mixture", *Sov. J. Plasma Phys.* **11**, 210 (1985)
- de Oliveira N., Roudjane M, Joyeux D, Phalippou D, Rodier J-C, Nahon L, "High-resolution broad-bandwidth Fourier-transform absorption spectroscopy in the VUV range down to 40 nm", *Nat. Photonics* **5**, 149 (2011)
- de Oliveira N, Joyeux D, Phalippou D, Rodier J C, Polack F, Vervloet M, Nahon L, "A Fourier transform spectrometer without a beam splitter for the vacuum ultraviolet range: From the optical design to the first UV spectrum", *Rev. Sci. Instr.* **80**, 043101 (2009)
- Dougar–Jabon V D, Velasco A J, Vivas F A, "Hydrogen negative ion production in an electron cyclotron resonance driven plasma", *Rev. Sci. Instrum.* **69**, 950 (1998)
- Dougra–Jabon V D, Reznikov D V, Santos Mayorga R, "Negative hydrogen ion ECR source", *Rev. Sci. Instrum.* **63**, 2529 (1992)
- Dougar–Jabon V D, "Production of Hydrogen and Deuterium Negative Ions in an Electron Cyclotron Resonance Driven Plasma", *Physica Scripta* **63**, 322 (2001)
- Eerden M J J, van de Sanden M C M, Otorbaev D K, Schram D C, "Cross section for the mutual neutralization reaction H<sub>2</sub><sup>+</sup> + H<sup>-</sup>, calculated in a multiple–crossing Landau-Zener approximation", *Phys. Rev. A.* **51**, 3362 (1995)
- Eley D D, Rideal E K, "Parahydrogen conversion on Tungsten", *Nature* **146**, 401 (1940)
- Fantz U, "Basics of plasma spectroscopy", *Plasma Sources Sci. Technol.* **15**, S137 (2006)

- Fantz U, Falter H, Franzen P, Wunderlich D, Berger M, Lorenz A, Kraus W, McNeely P, Riedl R, Speth E, "Spectroscopy – a powerful diagnostic tool in source development", Nucl. Fusion **46**, S297 (2006)
- Fantz U, Wunderlich D, "Franck-Condon factors, transition probabilities, and radiative lifetimes for hydrogen molecules and their isotopomers", At. Data Nucl. Data Tables **92**, 853 (2006)
- Firdman A, Kennedy L A, "Plasma Physics and Engineering", Taylors & Francis Books Inc., New York (2004)
- Friedl R, Kurutz U, Fantz U, "Efficiency of Cs-free materials for negative ion production in and plasmas", AIP Conf. Proc. **1869**, 030022 (2017)
- Friedl R, Rauner D, Heiler A, Fantz U, "Dissociative recombination and its impact on the line profile of the hydrogen Balmer series", Plasma Sources Sci. Technol. **29**, 015014 (2020)
- Gammino S, Celona L, Ciavola G, Maimone F, Mascali D, "Review of high current 2.45 GHz electron cyclotron resonance sources (invited)", Rev. Sci. Instrum. **81**, 02B313 (2010)
- Gavilan L, Lemaire J L, Vidali G, Sabri T, Jæger C, "The formation of molecular hydrogen on silicate dust analogs : The rotational distribution", Astrophys. J. **781**, 79 (2014)
- Gobin R, Auvray P, Bacal M, Breton J, Delferrière O, Harrault F, Ivanov Jr. A. A., Svarnas P, Tuske O, "Two approaches for H<sup>-</sup> ion production with 2.45 GHz ion sources", Nucl. Fusion **46**, S281 (2006)
- Godyak V A, Deminov V I, "Probe measurements of electron-energy distributions in plasmas: what can we measure and how can we achieve reliable results?", J. Phys. D: Appl. Phys. **44**, 233001 (2011)
- Gordiets B, Ferreira C M, Pinheiro M J, Ricard A, "Self-consistent kinetic model of low-pressure N<sub>2</sub>-H<sub>2</sub> flowing discharges: I. Volume processes", Plasma Sources Sci. Technol. **7**, 363 (1998)
- Graham W G, "The kinetics of negative hydrogen ions in discharges", Plasma Sources Sci. Technol. **4**, 281 (1995)
- Hall P I, Čadež I, Landau M, Pichou F, Schermann C, "Vibrational Excitation of Hydrogen via Recombinative Desorption of Atomic Hydrogen Gas on a Metal Surface", Phys. Rev. Lett. **60**, 337 (1988)
- Harris J, Kasemo B, "On precursor mechanisms for surface reactions", Surf. Sci. **105**, L281 (1981)
- Hiskes J R, "Cross sections for the vibrational excitation of the H<sub>2</sub>(X<sup>1</sup>Σ<sub>g</sub><sup>+</sup>) state via electron collisional excitation of the higher singlet states, J. Appl. Phys. **51**, 4592 (1980)
- Hiskes J R, Karo A M, "Analysis of the vibrational distribution in a hydrogen discharge", Appl. Phys. Lett. **54**(6), 508 (1989)
- Hiskes J R and Karo A M, "Recombination and dissociation of H<sub>2</sub><sup>+</sup> and H<sub>3</sub><sup>+</sup> ions on surfaces to form H<sub>2</sub>(v'): Negative-ion formation on low-work-function surfaces", J. Appl. Phys. **67**, 6621 (1990)
- Huq M S, Doverspike L D, Champion R L, "Electron detachment for collisions of H<sup>-</sup> and D<sup>-</sup> with hydrogen molecules", Phys. Rev. A. **27**(6), 2831 (1983)

- Jackson B, Lemoine D, "Eley–Rideal reactions between H atoms on metal and graphite surfaces: The variation of reactivity with substrate", *J. Chem. Phys.* **114**, 474 (2001)
- Janev R K, Reiter D, Samm U, "Collision Processes in Low-Temperature Hydrogen Plasma", Forschungszentrum, Zentralbibliothek (2003)
- Kammler Th., Kolovos-Vellianitis D, Küppers J, "A hot-atom reaction kinetic model for H abstraction from solid surfaces", *Surf. Sci.* **460**, 91 (2000)
- Kolasinski K W, "Surface Science: Foundations of Catalysis and Nanoscience", Wiley 4<sup>th</sup> Edition (2019)
- Komppula J, Tarvainen O, Kalvas T, Koivisto H, Kronholm R, Laulainen J, Myllyperkiö P, "VUV irradiance measurement of a 2.45 GHz microwave-driven hydrogen discharge", *J. Phys. D: Appl. Phys.* **48**, 365201 (2015)
- Kurutz U, Fantz U, "Investigations on cesium-free alternatives for H<sup>-</sup> formation at ion source relevant parameters", *AIP Conf. Proc.* **1655**, 020005 (2015)
- Kurutz U, Friedl R, Fantz U, "Investigations on Cs-free alternatives for negative ion formation in a low pressure hydrogen discharge at ion source relevant parameters", *Plasma Phys. Control. Fusion* **59**, 075008 (2017)
- Lacoste A, Lagarde T, Béchu S, Arnal Y, Pelletier J, "Multi-dipolar plasmas for uniform processing: physics, design and performance", *Plasma Sources Sci. Technol.* **11**, 407 (2002)
- Lagarde T, Arnal Y, Lacoste A, Pelletier J, "Determination of the EEDF by Langmuir probe diagnostics in a plasma excited at ECR above a multipolar magnetic field", *Plasma Sources Sci. Technol.* **10**, 181 (2001)
- Lemaire J L, Vidali G, Baouche S, Chehrouri M, Chaabouni H, Mokrane H, "Competing mechanisms of molecular hydrogen formation in conditions relevant to the interstellar medium" *Astro. Phys. J. Lett.* **725**, L156 (2010)
- Lieberman M A and Lichtenberg A J, *Principles of Plasma Diagnostics and Material Processing*, John Wiley & Sons, Inc. Publication, 2<sup>nd</sup> Edition, Hoboken, New Jersey (2005)
- Matveyev A A, Silakov V P, "Kinetic processes in a highly-ionized non-equilibrium hydrogen plasma", *Plasma Sources Sci. Technol.* **4**, 606 (1995)
- Miller K A, Bruhns H, Čížek M, Eliášek J, Cabrera-Trujillo R, Kreckel H, O'Connor A P, Urbain X, Savin D W, "Isotope effect for associative detachment:  $\text{H}(\text{D})^- + \text{H}(\text{D}) \rightarrow \text{H}_2(\text{D}_2) + \text{e}^-$ ", *Phys. Rev. A* **86**, 032714 (2012)
- Mitrou M, Svarnas P. Béchu S., "H<sup>-</sup> and D<sup>-</sup> production efficiency in a multi-dipole ECR-plasma source as a function of gas pressure", International Conference on Ion Sources (ICIS), 20-24 September 2021, Victoria, BC, Canada; online format (2021)
- Morisset S, Aguillon F, Sizun M, Sidis V, "Quantum dynamics of H<sub>2</sub> formation on a graphite surface through the Langmuir Hinshelwood mechanism", *J. Chem. Phys.* **121**, 6493 (2004)
- Mosbach T, "Population dynamics of molecular hydrogen and formation of negative hydrogen ions in a magnetically confined low temperature plasma", *Plasma Sources Sci. Technol.* **14**, 610 (2005)

- Peart B, Dolder K T, "Measurements of cross sections for the dissociative recombination of  $D_2^+$  ions", J. Phys. B: Atom. Molec. Phys. **6**, L359 (1973)
- Peart B, Dolder K T, "Collision between electrons and  $H_2^+$  ions VI. Measurements of cross sections for the simultaneous production of  $H^+$  and  $H^-$ ", J. Phys. B: Atom. Molec. Phys. **8**, 1570 (1975)
- Rauner D, Kurutz U, Fantz U, "Comparison of measured and modelled negative hydrogen ion densities at the ECR-discharge HOMER", AIP Conf. Proc. **1655**, 020017 (2015)
- Roth J R, *Industrial Plasma Engineering*, Institute of Physics Publishing Ltd., London (1995)
- Rutigliano M, Cacciatore M, Billing G, "Hydrogen atom recombination on graphite at 10 K via the Eley-Rideal mechanism", Chem. Phys. Lett. **340**, 13 (2001)
- Rutigliano M, Cacciatore M, Eley-Rideal recombination of hydrogen atoms on a tungsten surface Phys. Chem. Chem. Phys., **13**, 7475 (2011)
- Spence D, Lykke K R, "Production of negative hydrogen and deuterium ions in microwave-driven ion sources", Proc. 19<sup>th</sup> Linear Accelerator Conference (LINAC), Chicago, IL, USA, TU4048, 508 (1998)
- Svarnas P, Breton J, Bacal M, Mosbach T, "Pressure optimization for  $H^-$  ion production in an electron cyclotron resonance-driven and a filamented source", Rev. Sci. Instrum. **77**, 03A532 (2006)
- Svarnas P, Breton J, Bacal M, Faulkner R, "Plasma electrode bias effect on the  $H^-$  negative-ion density in an electron cyclotron resonance volume source", IEEE Trans. Plasma Sci. **35**, 1156 (2007)
- Taccogna F, Schneider R, Longo S, Capitelli M, "Modeling of a negative ion source. I. Gas kinetics and dynamics in the expansion region", Phys. Plasmas **14**, 73503 (2007)
- Velasco A J C, Parra A L C, Serrano W A P, "Negative Ion Generation and Isotopic Effect in Electron Cyclotron Resonance Plasma", IEEE Trans. Plasma Sci. **43**, 1729 (2015)
- Williamson M C, Lichtenberg A J, Lieberman M A, "Self-consistent electron cyclotron resonance absorption in a plasma with varying parameters", J. Appl. Phys. **72**, 3924 (1992)
- Wood B J, Wise H, "Diffusion and Heterogeneous Reaction. II. Catalytic Activity of Solids for HydrogenAtom Recombination" J. Chem. Phys. **29**, 1416 (1958)
- Wood, B. J., Wise, H., "Kinetics of hydrogen aton recombination on surfaces" J. Phys. Chem. **65**, 1976 (1961)
- Yang W, Averkin S N, Khrabrov A V, Kaganovich I D, Wang Y N, Aleiferis S, Svarnas P, "Benchmarking and validation of global model code for negative hydrogen ion sources", Phys. Plasmas **25**, 113509 (2018)
- Zhang T, Peng S-X, Wu W-B, Ren H-T, Zhang J-F, Wen J-M, Ma T-H, Jiang Y-X, Sun J, Guo Z-Y, Chen J-E, "Practical 2.45-GHz microwave-driven Cs-free  $H^-$  ion source developed at Peking University", Chin. Phys. B **27**, 105208 (2018)